Catalysis Communications 175 (2023) 106609

Contents lists available at ScienceDirect

Catalysis Communications

journal homepage: www.elsevier.com/locate/catcom

Core-shell Bi-containing spheres and TiO_2 nanoparticles co-loaded on kaolinite as an efficient photocatalyst for methyl orange degradation

Chen Li [a], Li Sun [a], Jinan Niu [a,*], Arianit A. Reka [b], Peizhong Feng [a,*], Hermenegildo Garcia [c,*]

[a] School of Materials Science and Physics, China University of Mining and Technology, Xuzhou 221116, China
[b] Faculty of Natural Sciences and Mathematics, University of Tetova, Tetovo 1200, North Macedonia
[c] Instituto de Tecnologia Quimica CSIC-UPV, Universitat Politecnica de Valencia, Valencia 46022, Spain

ARTICLE INFO

Keywords:
Kaolinite
TiO_2
Bi spheres
Photocatalysis
Clay substrate
Type II heterojunction

ABSTRACT

Improving the efficiency/cost ratio is the key to the practical application of photocatalysts. Using cheap minerals as carriers is an effective means to improve the efficiency/cost ratio of photocatalysts. Here, kaolinite was used to co-load TiO_2 nanoparticles and Bi containing core-shell spheres forming the composites with excellent photocatalytic performance. The rate constant per unit mass of TiO_2 in the optimal sample reached 18 times that of TiO_2. Kaolinite plays important roles in promoting photocatalytic activity by improving the dispersion of TiO_2 and the adsorption of O_2 molecules and MO anions, besides the type-II energy band alignment of TiO_2 and Bi_xO_y.

1. Introduction

With the advancement of industrialization, the human society's demand for resources is increasing, and environmental and energy problems are becoming more and more serious [1]. As a renewable energy, solar energy is increasingly becoming an important primary energy source. In recent years, it has been widely used in the fields of organic matter degradation, reduction of toxic hexavalent species, and hydrogen production from water splitting, carbon dioxide reduction, and nitrogen reduction to ammonia production. In these applications, the key is to develop efficient semiconductor photocatalysts. The most common semiconductor catalysts include TiO_2 [2,3], ZnO [4,5], CdS [6,7] and so on.

TiO_2 is widely used in photocatalysis because of its efficient photo-induced charge separation, good stability, low cost and non-toxicity. Unfortunately, TiO_2 has a wide bandgap of about 3.2 eV [8,9], so the photocatalytic reaction on TiO_2 can only be excited by ultraviolet light, which only accounts for a small proportion of solar energy, about 5% [10]. Moreover, TiO_2 nano-powders are easy to agglomerate, leading to the decrease of their specific surface area, which limits its practical application in photocatalysis.

Precious metal deposition is an effective means to improve the photocatalytic activity of TiO_2, and the most studied precious metals includes Au, Ag and Cu with significant plasmon resonance (PR) effect [11,12]. Bismuth, as a non-precious, main group element, has recently been found to have a similar PR effect but with a lower cost. Bi particles have been successfully used to modify TiO_2 [13], $CaWO_4$ [14], Bi_2WO_6 [15] and ZnO [16], which exhibited excellent photocatalytic performance. In addition, Bi oxides (such as α-Bi_2O_3) are also important semiconductor oxides with the bandgaps in the range of 2–3.9 eV [17]. However, the photocatalytic efficiency of bismuth oxide is low, mainly due to the faster recombination of photogenerated charge carriers [18,19]. Using other semiconductors to couple with bismuth oxide can construct heterojunction and effectively improve the photocatalytic performance of bismuth oxide. At present, some heterojunction photocatalysts such as LDH/Bi_2O_3 [20,21], C_3N_4/Bi_2O_3 [22,23], $BiVO_4$/Bi_2O_3 [24] and h-BN/Bi_2O_3 [25] have been successfully synthesized.

Loading TiO_2 on the support surface is an efficient means to reduce the agglomeration of TiO_2. Typical supports include activated carbon [26], carbon fiber [27], glass fabric [28], FTO conductive glass [29] and molecular sieves [30]. Most of these supports can achieve good TiO_2 recovery from the reaction medium. However, these supports belong to synthetic materials with comparative high-cost, limiting their practical use. Natural silicate minerals such as kaolinite, montmorillonite and palygorskite are abundant, inexpensive and environmentally friendly materials [31–35]. Among them, kaolinite with a chemical formula of $Al_2Si_2O_5(OH)_4$ is widely used in paper, ceramic, coating and refractory fields due to its unique flake shape, good whiteness, excellent chemical stability, satisfying fire resistance and low price [36]. With the development of new technologies, kaolinite's application scope is constantly

* Corresponding authors.
E-mail addresses: jinan.niu@cumt.eud.cn (J. Niu), pzfeng@cumt.eud.cn (P. Feng), hgarcia@qim.upv.es (H. Garcia).

https://doi.org/10.1016/j.catcom.2023.106609
Received 1 November 2022; Received in revised form 4 January 2023; Accepted 12 January 2023
Available online 13 January 2023

expanding, for example, it can be used as polymer composite filler [37,38], defect regulator [39,40], adsorbent [41], nanofluidic membranes [42,43] and photocatalyst carrier [44,45]. In terms of photocatalysis, for example, Zyoud et al. [46] prepared ZnO/kaolinite composite by directly growing ZnO nanoparticles on kaolinite surface, the results showed that the composite exhibited higher photocatalytic efficiency in the degradation of 2-chlorophenol. Kočí et al. [47] prepared kaolinite/titania composites by using thermal hydrolysis of kaolinite and titanyl sulphate ($TiOSO_4$) suspension, which gave a higher yield of methane and methanol as CO_2 photocatalytic reduction products than commercial P25 TiO_2. Xu et al. [48] prepared the kaolinite/TiO_2 composites by using sol-gel method and subsequent calcination, and compared the effect of the intercalation-exfoliation and the acid-treatment on degrading the methylene blue and phenol in water. Cheng et al. [49,50] used a simple hydrothermal approach to prepare the kaolinite/BiOI composite which showed excellent photocatalytic activity for RhB degradation under visible light irradiation; by the similar strategy, they prepared a kaolinite/$MnFe_2O_4$ composite to activate peroxodisulfate, leading to the efficient degradation of chlortetracycline hydrochloride.

Sun et al. [51–53] synthesized a novel TiO_2/kaolinite composite with oxygen vacancies and surface defects by a mild sol-gel method combining with nitrogen promotion, which showed an enhanced photocatalytic activity in the degradation of ciprofloxacin. Using the sol-gel approach associated with chemical stripping and self-assembly, a g-C_3N_4/TiO_2/kaolinite composite was also fabricated exhibiting an enhanced visible light activity. The same group prepared the $CuFe_2O_4$/kaolinite composite catalyst through the citrate combustion method, displaying the good efficiency to activate peroxymonosulfate for the destruction of bisphenol A. Yang et al. [40,54] successfully synthesized a kaolinite-induced defective graphitic carbon nitride catalyst via intercalation and in-situ calcination, and the obtained catalyst showed the excellent degradation performance for Orange II dye under visible light irradiation due to its special structure and the appearance of synergistic effects; they also used a rod-like kaolinite to support ZnO nanoparticles through a thermal treatment, and the obtained Pd-ZnO/kaolinite showed good photocatalytic activity for the degradation of methylene blue. For a comprehensive description of the research progress in the field of kaolinite-based photocatalysis, there are several good reviews for further investigations [55–62]. However, no composite photocatalyst with TiO_2 and metal Bi or bismuth oxide supported on the surface of kaolinite has been reported so far.

In this work, a novel kaolinite/TiO_2/Bi containing core-shell sphere composite (KTB) with good photocatalytic activity has been successfully prepared by a simply hydrothermal-solvothermal method, and the effect of different kaolinite-TiO_2 (KT) additions on the morphology and structure of KTB composites have been systematically studied. In addition, the photocatalytic performance of KTB samples for methyl orange degradation in water has been studied in detail, observing a unique contribution of kaolinite substrate to the photocatalytic enhancement effect and the band energy matching of each component of KTB.

2. Experimental

2.1. Materials

Kaolinite (K) with high purity was purchased from Maoming in Guangdong Province of China， isopropanol (IPA), titanium tetraisopropanolate (TTIP), $Bi(NO_3)_3{\cdot}5H_2O$, nitric acid, ethanol, methyl orange (MO), ammonium oxalate (AO), ethylene glycol (EG), methanol and Na_2SO_4 were purchased from Sinopharm (Shanghai, China), 1,4-benzoquinone (BQ) and polyvinyl pyrrolidone (PVP) were from Aladdin (Shanghai, China). All reagents are chemically pure and used without further purification.

2.2. Preparation

2.2.1. Synthesis of KT

Firstly, 1 mL TTIP, 5 mL 2 M nitric acid and 15 mL IPA were mixed and stirred for 1 h at room temperature until the solution becomes transparent. Next, 1 g kaolinite and deionized water were added into solution to a total volume of 250 mL, and stirred for 2 h. Finally, the solution was heated to 65 °C for another 24 h. After the reaction, the white precipitate was separated by centrifugation (5000 rpm, 3 min), washed for three times with deionized water and ethanol alternately, and then dried at 80 °C overnight. The prepared kaolinite-TiO_2 composite was denoted as KT.

2.2.2. Synthesis of KTB

Firstly, 0.36 g of $Bi(NO_3)_3$ $5H_2O$ was dissolved in 10 mL of 1 M HNO_3. Next, 55 mL EG and 0.6 g of PVP were added into solution and stirred for 1 h. Then, 0.15, 0.3, 0.6, 1.2 g KT were added into solution respectively and stirred for 1 h. Finally, the mixed solution was transferred into the autoclave and heated at 160 °C for 15 h. After the reaction, the dark gray precipitate was separated by centrifugation (5000 rpm, 3 min), washed for three times alternately with deionized water and absolute ethanol, and then dried at 60 °C for 12 h. A series of kaolinite-TiO_2-Bi composites with different KT contents, denoted as 0.15KTB, 0.3KTB, 0.6KTB, 1.2KTB (corresponding to 0.15, 0.3, 0.6, 1.2 g KT, separately) was obtained (Fig. 1).

2.2.3. Synthesis of reference samples

To compare the photocatalytic mechanism of KTB composites, TiO_2/Bi composites (TB) and Bi spheres (B) samples were also prepared separately. The steps for preparing the TB were similar to those of KTB, the only difference was that the KT added in the solution was replaced with 0.16 g TiO_2. When preparing B, no KT or TiO_2 was added to the solution, and the other steps were exactly the same.

2.3. Characterization

The phases of the obtained samples were characterized by X-ray diffraction (XRD, D8 Advance, Bruker) with Cu Kα radiation at 40 kV and 30 mA and a scanning speed of 5°/min. The morphology was examined by field emission scanning electron microscopy (FESEM, UHR SU8220, Hitachi) and high resolution transmission electron microscopy (HRTEM, Tecnai G2 F20, FEI). Nitrogen adsorption–desorption isotherms were measured with the ASAP 2020 plus HD 88 system (Micromeritics). The Brunauer–Emmett–Teller (BET) method was used to calculate the specific surface area (SSA) and the Barrett-Joyner-Halenda (BJH) method was used to calculate the pore size distribution (PSD) curve. The bonding states of elements and the valence band spectra were analyzed by X-ray photoelectron spectroscopy (XPS, Escalab 250Xi, Thermo Scientific) and the C1s 284.8 eV peak was used as reference. The content of TiO_2 in KBT was analyzed by inductively coupled plasma optical emission spectrometer(ICP-OES, Agilent 5110). The diffuse reflectance absorption spectrum (DRS) was measured by using a fiber optic spectrometer (HR3000-Pro, Jingyi Electronic Science & Technology Co., Ltd., Guangzhou, China) equipped with an external integrating sphere and a $BaSO_4$ standard whiteboard. A fluorescence spectrophotometer (FS5, Edinburgh, UK) was used to record photoluminescence (PL) spectra at excitation wavelength of 315 nm. Photocatalytic tests were carried out using a PL-03 multi-station photochemical reactor (Prince, Beijing) with a distance of 9 cm between the central water-cooled light source and the surrounding quartz reaction tubes (Fig. S1). Electrochemical properties were tested by using a electrochemical workstation (RST5200F) from Shiruisi (Suzhou, China).

2.4. Photocatalytic tests

The photocatalytic activity of the samples was evaluated by

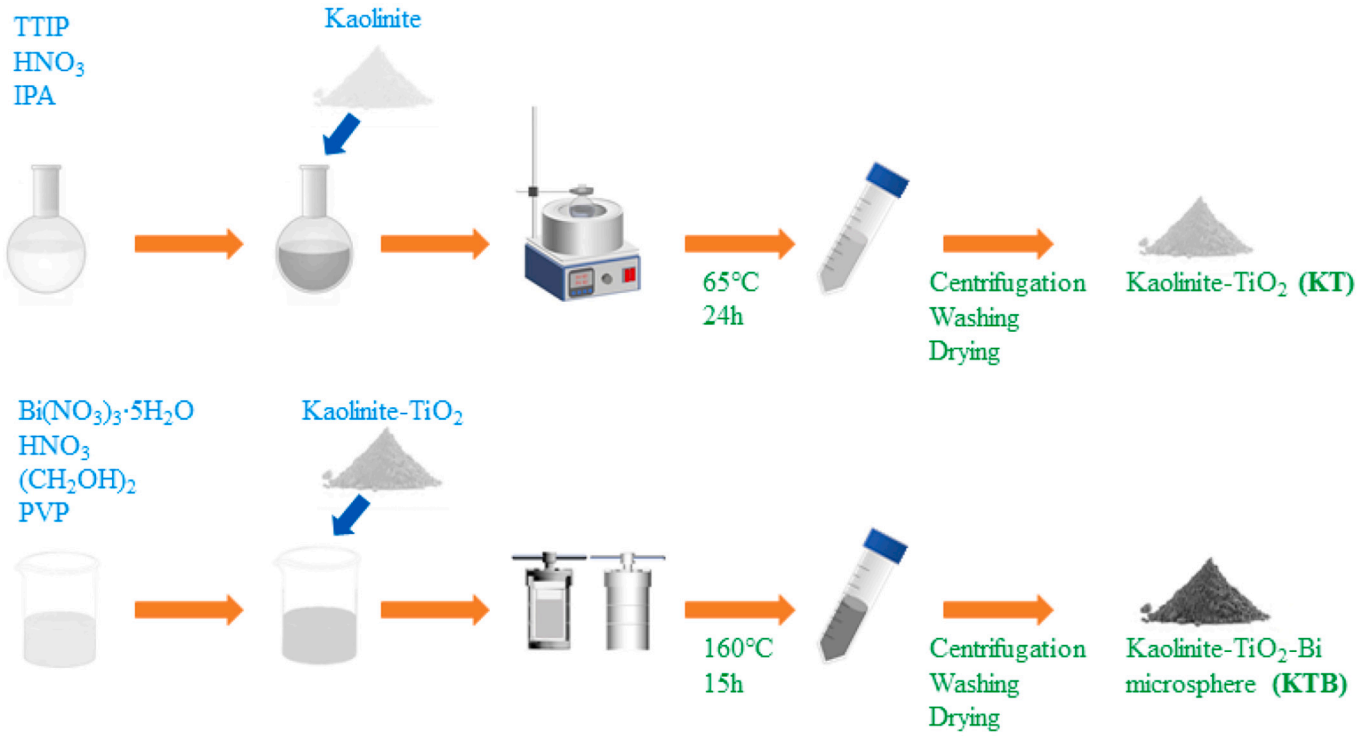

Fig. 1. Scheme of preparation route of KTB composites.

degrading MO dye under low-intensity xenon lamp source (Shanghai Jiguang Special Lighting, 200 W). The radiation spectrum is shown in Fig. S2 and the actual irradiation intensity was measured to be 0.4 kW/m^2 at the position of reaction tube using a TM-207 solar power meter produced by TENMARS. 40 mg of the sample was dispersed in 40 mL of MO solution with a concentration of 20 mg/L, and the suspension was pre-stirred in the dark for 1 h to achieve the adsorption-desorption equilibrium of the catalyst for MO molecules. The photodegradation reaction was carried out under the irradiation of 200 W xenon lamp, the total irradiation time was 3 h. In the reaction, 4 mL of suspension was taken out every 30 min, then the supernatant was separated by centrifugation (10,000 rpm for 3 min), and tested at the wavelength of 464 nm to obtain the absorbance of MO in the supernatant. In addition, the total organic carbon (TOC) of the MO solution was determined by a TOC analyzer (Multi N/C 3100, Jena).

To gain information on the photocatalytic mechanism, a series of active species trapping experiments were performed. IPA was used to trap hydroxyl radicals (·OH), AO to quench holes (h^+), and BQ to capture superoxide ion ($\cdot O_2^-$). The concentration of each trapping agent is as follows: 10 mmol/L for IPA, 6 mmol/L for AO, and 0.1 mmol/L for BQ [63].

2.5. Electrochemical measurements

The electrochemical workstation was used to obtain photocurrent response plots (0.6 V bias potential and 30 s interval between light on and off), electrical impedance spectroscopy (1 MHz ~ 0.01 Hz, 10 mV amplitude) and Mott-Schottky plots (1000 Hz, 10 mV amplitude). A three electrode system was used in this experiment. The platinum plate was used as the counter electrode, the Ag/AgCl electrode was used as the reference electrode, and the electrolyte was 0.1 M Na_2SO_4 solution. The working electrode was made as follows: 0.5 mL of water/isopropanol mixed solution (water: isopropanol = 3:1), 10 μL of Nafion solution and 5 mg of catalyst were mixed and sonicated for 0.5 h. Then 20 μl mixed solution was evenly spread onto the 2 × 2 cm^2 ITO conductive glass and dried at 60 °C for use.

3. Results

3.1. XRD analysis

The XRD spectra of each sample are shown in Fig. 2a. For sample B, the diffraction peaks at 22.47, 27.16, 37.95, 39.62, 44.55, 45.87, 46.02 and 48.69° correspond respectively to the (003), (012), (104), (110), (015), (006), (113) and (202) lattice spacing of metal bismuth (PDF#44–1246). These peaks are quite sharp, indicating the good crystallinity of metal Bi phase in sample B. After B coupled with TiO_2 (TB), an obvious peak at 25.3° can be seen, corresponding to anatase TiO_2 (101) plane, besides metallic Bi characteristic peaks. Sample K only has characteristic diffraction peaks of kaolinite phase, and no other impurity peaks can be clearly found, showing the high purity of sample K. The main peaks at 12.40, 19.88, 20.35, 21.35, 23.15, 23.84, 24.95, 26.43, 35.07, 35.54, 36.07, 38.56, 39.38, 41.37, 45.67, 55.32 and 62.50° correspond to the (001), (020), (−110), (−1−11), (0−21), (021), (002), (111), (−201), (−1−31), (200), (−202), (131), (−220), (−203), (−151) and (−331) planes, respectively (PDF# 75–1593). The pure TiO_2 sample shows the typical characteristic of anatase phase (PDF#21–1272) with broadened diffraction peaks (Fig. S3) led by the small size of TiO_2 nanoparticles (Fig. S4). The XRD pattern of kaolinite-TiO_2 composite (KT) is similar to that of kaolinite (Fig. 2b). However, after normalizing the intensity of kaolinite (002) peaks in K and KT, and further enlarging the local range of 24–30°, it can be clearly seen that the intensity of the 25.3° peak of KT increases relative to that of K, and this peak is even clearer for sample TB, corresponding to the diffraction peak of anatase TiO_2 (101) plane, which confirms the successful loading of TiO_2 on kaolinite and successful combination between TiO_2 and B. The results are consistent with that in literature [64]. The co-loading of B and TiO_2 on kaolinite was performed by the loading of Bi on the KT sample (KTB), observing a metal Bi (012) peak (Fig. 2c), suggesting the successful load of B component on KT. After normalization of K (002) peak, the (012) peak intensity of metal Bi gradually increases in the order of 1.2KTB < 0.6KTB < 0.3KTB < 0.15KTB. In addition, noted that the background in the range of 22–35° is significantly enhanced after the

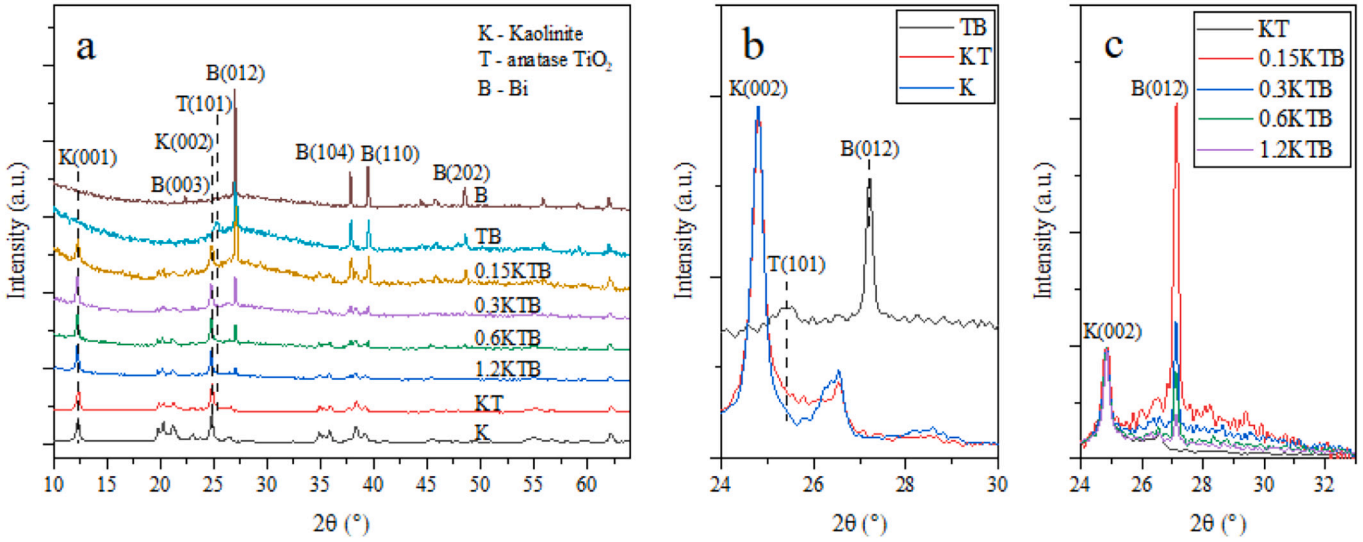

Fig. 2. (a) XRD patterns of the samples; (b) local comparison at the range of 24–30° for K, KT and TB; (c) local comparison at the range of 24–30° for of KT and KTB.

addition of Bi, clearly indicating that some amorphous Bi compounds might also be formed in sample B, which can be further determined by the HRTEM and XPS tests. At the same time, the characteristic peaks of kaolinite and TiO_2 did not shift significantly after further loading B, which suggests that the addition of Bi should not affect the structure of KT complex significantly in the loading process adopted in this work.

3.2. SEM and mapping analysis

The SEM images of samples are shown in Fig. 3. The original kaolinite particles are typical hexagonal flakes with a size of about 200 nm - 2 μm and a relatively smooth surface (Fig. 3a). After loading TiO_2, the shape of kaolinite flakes did not change significantly, but the surface roughness increased significantly, and many fine nanoparticles were formed (Fig. 3b). According to the XRD results, it can be concluded that these nanoparticles are TiO_2 which were successfully loaded on kaolinite. Sample B exhibits a microsphere-like morphology with a size of 50–200 nm (Fig. 3c), which is significantly smaller than that of the kaolinite flakes, thus facilitating its formation on the kaolinite surface. In TB composite, the round B microspheres were loaded in fine TiO_2 nanoparticle clusters (Fig. 3d). Further element mapping test results show that the nanoparticle aggregates correspond to the distribution of Ti and O elements, while the spherical region presents obvious concentration of Bi elements (Fig. S5). Therefore, it can be proved that the bigger spherical particles are B spheres and the nanoparticle aggregates are TiO_2 aggregates in sample TB. After the KT composite was further loaded with B (KTB), in addition to fine TiO_2 nanoparticles, B spheres also appeared on the surface of kaolinite (Fig. 3e-h); and the B spheres gradually decreased with the increase of KT/Bi ratio. The results clearly demonstrate the successful formation of KTB composites. It is also noted that when Bi addition is high, B spheres tended to aggregate together (Fig. 3e and f). This may reduce the number of active sites on the surface of the B spheres and increase the recombination of photogenerated carriers in B, which is not conducive to the full improvement of the photocatalytic performance for KTB composite.

Fig. 4 shows the element distribution mapping of sample 1.2KTB. There is an obvious circular sphere distributed on the flake particles in this part. In the individual scanning diagram of each element, O, Si and Al have the same distribution as the flake particles, corresponding to the kaolinite grains. The distribution of Ti element is relatively diffuse, which on the one hand suggests that Ti is uniformly distributed, and on the other hand reflecting its low content which can be further confirmed from the small EDS peak in Fig. 4i. The distribution of Bi element is mainly in the spherical region, further indicating that B spheres were successfully compounded with KT.

3.3. TEM analysis

Fig. 5a gives the TEM image of kaolinite, which shows the pseudo-hexagonal flakes consistent with the SEM results, with a relatively smooth surface. When TiO_2 was loaded, many fine particles were added to the surface of kaolinite (Fig. 5b). Combined with the XRD results, it showed that the TiO_2 was successfully loaded on kaolinite. The HRTEM image of pure TiO_2 shows the aggregation of nanocrystals of about 5 nm (Fig. S4a). The fringe of 0.35 nm is consistent with the (101) plane of anatase TiO_2, and the diffraction rings for the agglomeration also correspond to (101), (004), (200), (211) and (204) planes of anatase TiO_2, respectively (Fig. S4b), further proving that the nanoparticles on K is anatase TiO_2. After further loading of B, larger-sized Bi spheres also appeared on the surface of kaolinite (Fig. 5c). HRTEM of the marked red rectangular area in Fig. 5c shows the lattice fringes of 0.395 and 0.33 nm in the microspheres, corresponding to the (003) and (012) spacing of metal Bi [65], proving the existence of metallic Bi. Noted that a thin shell layer with a thickness of 1–3 nm appeared on the periphery of the sphere, and no obvious lattice fringe appeared in this area, probably caused by a small amount of amorphous bismuth oxide (Bi_xO_y) layer formed by the oxidation of the surface of Bi sphere during the synthesis process. A similar phenomenon has also been observed in an earlier study on the synthesis of Bi spheres [65]. The results indicate that the synthesized spheres have a core-shell structure with the surface layer of amorphous Bi_xO_y and the inner core of metallic Bi. In order to avoid confusion with these two substances, the microsphere sample is referred to as B for short. In addition, lattice fringe of 0.35 nm was also found in an adjacent microdomain outside the microsphere, corresponding to the (101) lattice spacing of anatase TiO_2 [66]. The TEM results clearly indicate the successful preparation of KTB composite.

3.4. N_2 adsorption-desorption analysis

The nitrogen adsorption–desorption isotherms of three representative samples (K, KT and 1.25KTB) are shown in Fig. 6. The adsorption isotherm of three samples show typical Type II characteristic according to the IUPAC classification indicating the nonporous nature. The hysteresis loop of desorption isotherm in the high relative pressure range is minor corresponding to the capillary condensation between particles which is the typical future of clay-based materials (Fig. 6a). The PSD

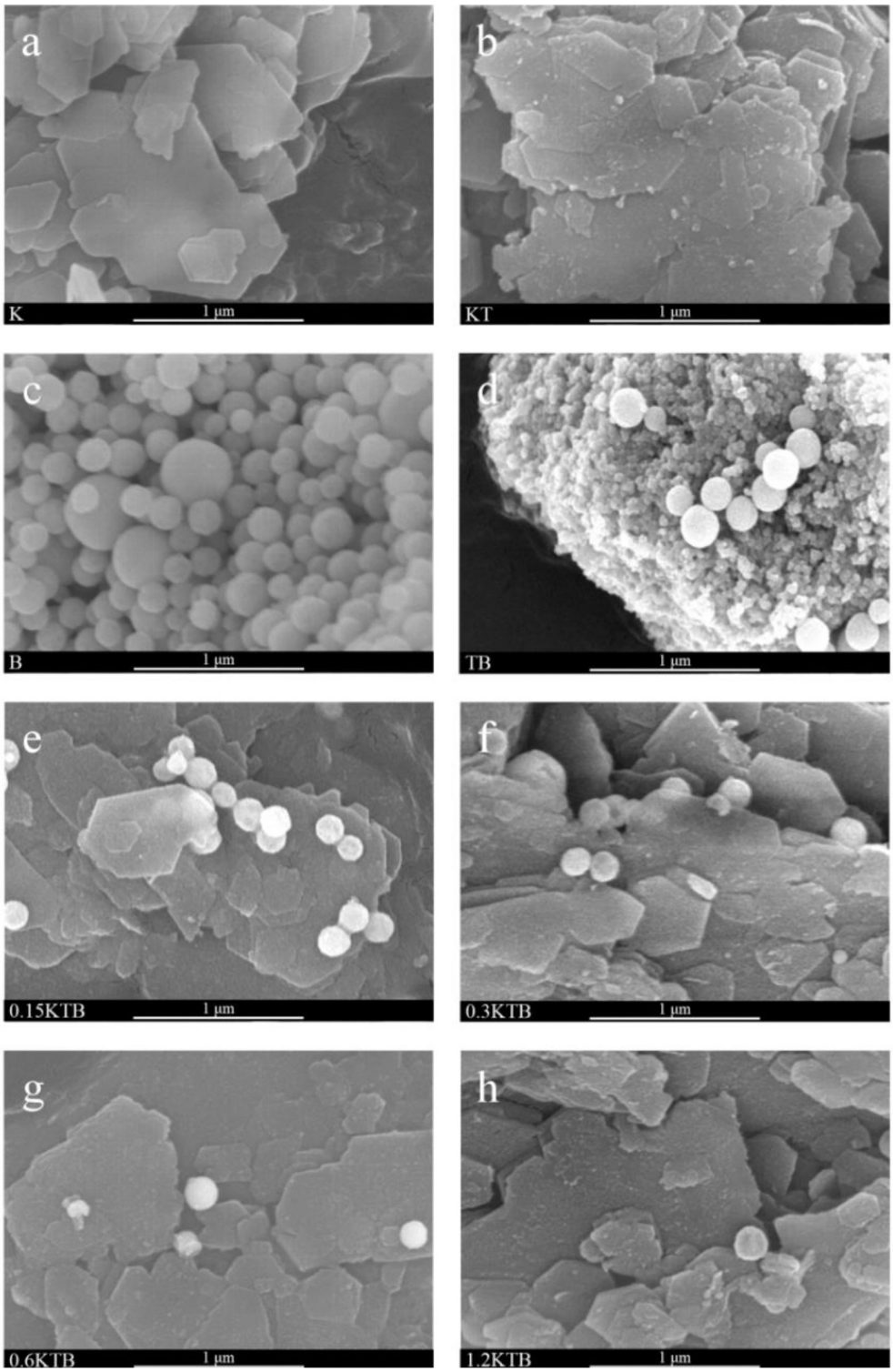

Fig. 3. SEM images of the samples. (a) K; (b) KT; (c) B; (d) TB; (e) 0.15KTB; (f) 0.3KTB; (g) 0.6KTB; (h) 1.2KTB.

curves of three samples calculated by the Barrett-Joyner-Halenda (BJH) method (Fig. 6b) show a main peak centered at 4 nm which is caused by tensile strength effect (TSE) [67]. No other obvious pores are found. The isotherm of KT shifts upward compared to that of K, indicating the increase of nitrogen adsorption capacity which can be led by the load of nano TiO_2. After further loading B spheres, the isotherm of obtained 1.2KTB shifts downward slightly compared to that of KT, suggesting the reducing nitrogen adsorption capacity caused by large B spheres. The PSDs in the range below 20 nm with the same trend further prove the isotherm results, as well as the changing of the SSA values (18.03, 63.19 and 22.16 m^2/g) for K, KT and 1.2KTB.

3.5. XPS analysis

The XPS survey spectrum and the narrow spectrum of each element of sample 1.2KTB are shown in Fig. S6 and Fig. 7, respectively. Both of Al and Si in kaolinite are connected with oxygen atoms through octahedral coordination and hexahedral coordination, respectively, showing sharp

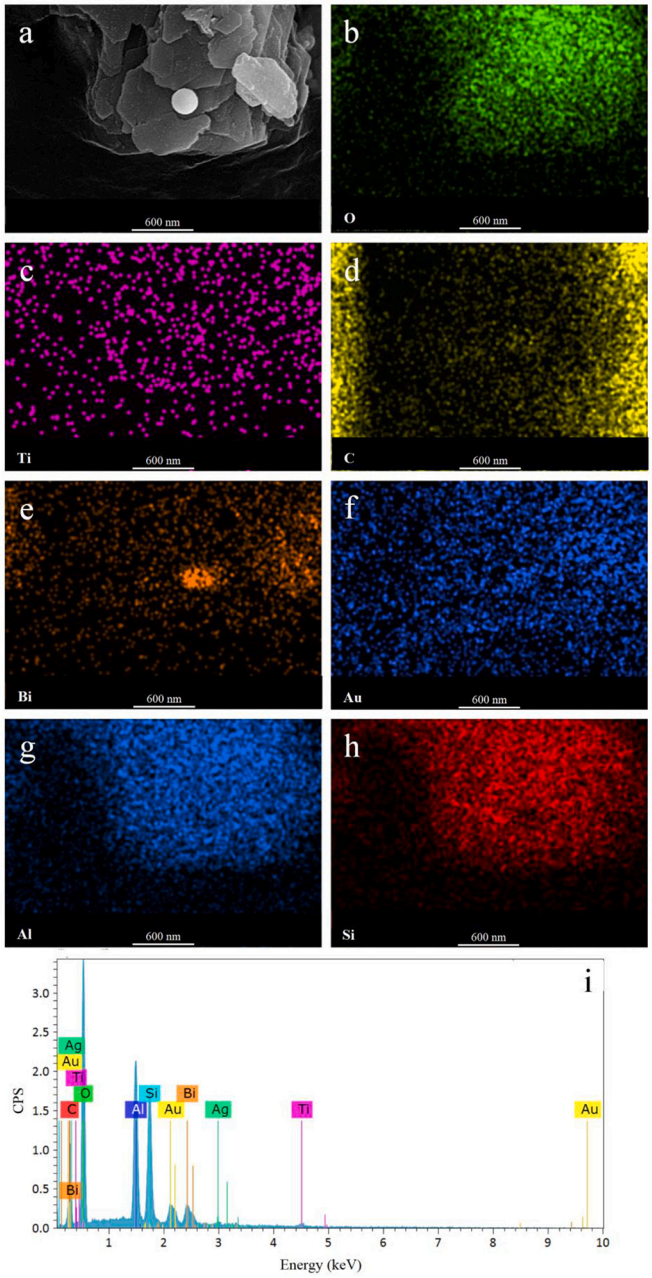

Fig. 4. (a-h) Element distribution mapping of sample 1.2KTB; (f) the corresponding EDS analysis.

XPS peaks (Fig. 7a and b). The appearance of C element in XPS is mainly due to adventitious carbon. The peak at 284.8 eV corresponds to C—C bond, the peak at 286.05 eV corresponds to C—O bond, and the 288.31 eV peak corresponds to C═O bond [68–70] (Fig. 7c). When decomposing the XPS peak of oxygen (Fig. 7d), in addition to the bonding state with Al, Si, and C elements, the bonds to Ti and Bi elements were also considered as shown in Fig. 7e and f. In the XPS peak of titanium element, Ti $2p_{1/2}$ peak has obvious broadening and enhancement, mainly caused by the interference of the 4d3 peak of Bi element. The 458.63 and 464.63 eV peaks correspond to the $2p_{1/2}$ and $2p_{3/2}$ peaks of Ti in TiO_2, while the 461.46 and 467.46 eV peaks correspond to the $2p_{1/2}$ and $2p_{3/2}$ peaks of Ti^{3+}, mainly caused by surface unsaturated titanium atoms or internal titanium atoms linked oxygen vacancies [71], leading to the generation of defect energy levels. The peaks at 463.49 and 465.92 eV correspond to the interference peaks caused by Bi $4d^3$ of metallic Bi in core and oxidized Bi in shell, respectively [72]. This can be more clearly seen by comparing the narrow scan results of Bi-containing samples (B, TB and KTB) and Bi-free samples (K and KT) in the range of 448–475 eV (Fig. S7).

The narrow scanning of Bi element presents two distinct valence states (Fig. 7f), where 157.26 and 162.48 eV correspond to the $4f_{7/2}$ and $4f_{5/2}$ peaks of metallic Bi, respectively [73]; while 159.29 and 164.58 eV correspond to the $4f_{7/2}$ and $4f_{5/2}$ peaks of Bi in Bi_xO_y, respectively [74]. In the XPS results of O element, 531.6 and 532.7 eV correspond to O—Al bond and O—Si bond in kaolinite [75], while 531.9 and 533.94 eV correspond to O—C bond and O═C bond caused by contaminating carbon [68–70]. The 530.01 eV peak corresponds to the O—Bi bond [74], and the 530.13 eV peak belongs to the O—Ti bond [71]. The XPS results clearly show that some Bi atoms in KTB are in metallic state and some are in oxidized state, which is consistent with the XRD and TEM results; in addition, there are obviously some titanium atoms in the low-coordination defect state, which may reduce the width of the bandgap of TiO_2, thereby improving light absorption.

In order to obtain the energy band matching relationship among K, T and B and further determine the mechanism of photogenerated carrier transfer of KTB composite, the valence band spectra of K, T and B were also measured, respectively. The results are shown in Fig. 8a-c. It can be seen that energy difference ($\Delta E_{f\text{-}V}$) from the valence band maximum (VBM) of kaolinite to Fermi level (E_{fermi}) is 4.16 eV ($\Delta E_{f\text{-}V} = E_{fermi} - E_{VBM}$) [76], while the $\Delta E_{f\text{-}V}$ of TiO_2 and B samples are 2.69 and 1.52 eV, respectively. As we all know, the measurement depth of XPS technique is only a few nanometers from the surface. From the TEM image, the range of a few nanometers on the surface of sample B is mainly amorphous bismuth oxide, so the valence band spectrum of sample B will mainly reflect the energy band properties of this oxide shell. Overall, based on the above $\Delta E_{f\text{-}V}$ results and the bandgap energy measurement results, it is possible to further determine the energy band matching relationship of K, T and Bi_xO_y components that actually function in KTB.

As a typical insulator, kaolinite has a wide bandgap which may exceed the lowest measurement limit of common UV–Vis spectrophotometers [77]. Therefore, DRS measurements cannot give the reliable bandgap energy of kaolinite. However, the bandgap energy can be obtained by using the difference between the energy of core-level peak and the onset of inelastic loss for O1s in kaolinite [78]. The obtained bandgap energy of kaolinite is 8.32 eV (Fig. 8d), close to 8.2 eV calculated by the G0W0 method using first-order perturbation theory [77]. According to the calculation of $\Delta E_{f\text{-}V}$, the Fermi level of kaolinite can be determined to be in the middle of the bandgap. This result demonstrates the nature of intrinsic insulator for kaolinite. Because sample B is a mixture and some TiO_2 contains a part of the defect state, their bandgaps determined by the XPS method have a large error, so their bandgaps are still obtained by the DRS optical method.

3.6. Optical absorption analysis

The DRS plots of samples are shown in Fig. 9a. Kaolinite has weak absorption in the whole spectral range with no obvious absorption edge. After loading TiO_2, the absorption in the ultraviolet part was enhanced, which corresponds to the UV absorption region of pure TiO_2. Sample B has strong absorption in the whole spectrum, especially in the ultraviolet region. Combined with the reported results [65], the strong absorption in the ultraviolet range can be mainly attributed to bismuth oxide, and the flat absorption in the visible to near-infrared range can be mainly attributed to metallic Bi, while a distinct absorption edge between these two range corresponds to the bandgap energy of sample B with the unique core-shell structure. By plotting $(\alpha h\upsilon)^{1/n}$ against $h\upsilon$ according the Tauc-plot method, the bandgap energy E_g can be determined from the intercept of the straight portion of the curve, where α is the absorbance coefficient presented in the equivalent absorption Kubelka-Munk units, υ is the frequency of absorbed light, h is Planck's constant, $n = 0.5$ related to the direct transition, and $n = 2$ related to the indirect transition. Anatase TiO_2 is an indirect semiconductor, and amorphous

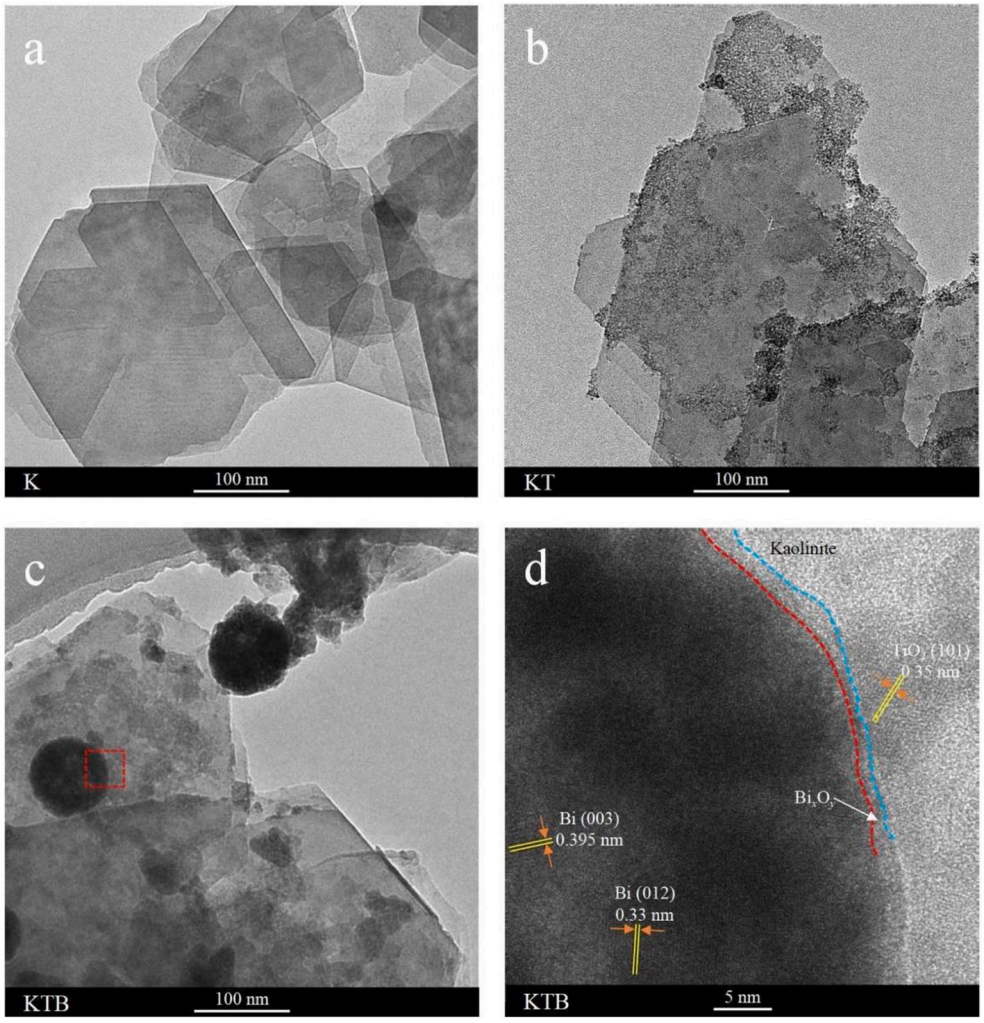

Fig. 5. Local TEM of sample 1.2KTB.

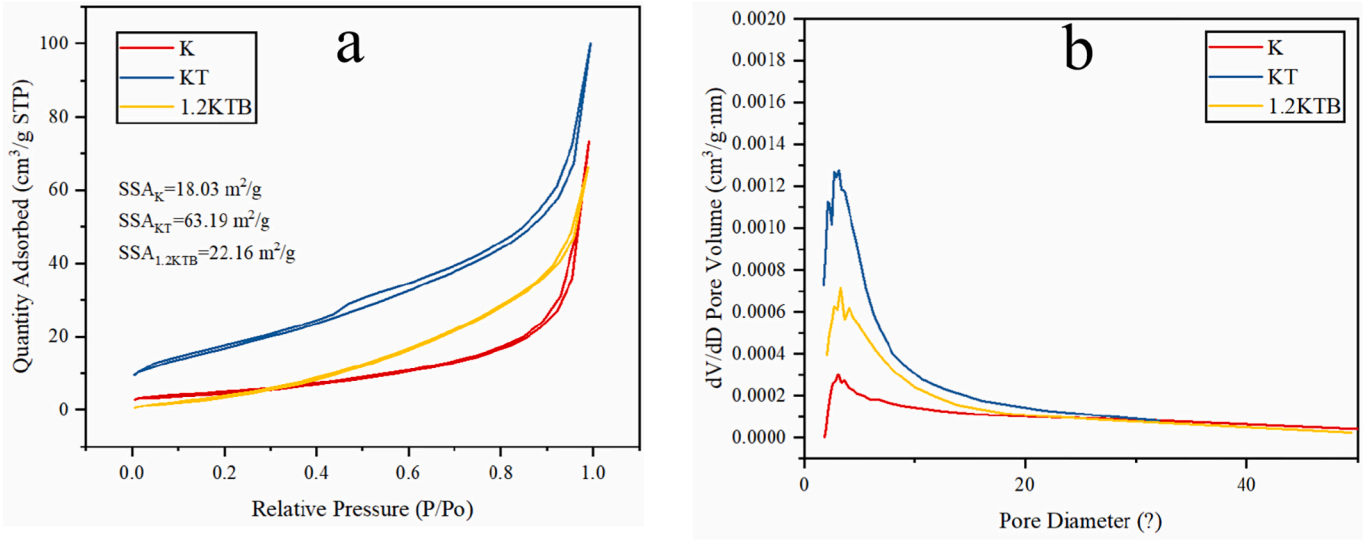

Fig. 6. Nitrogen adsorption–desorption isotherms, special surface area (SSA) (a) and pore size distributions (PSDs) (b) of three representative samples.

bismuth oxide is also considered to be dominated by indirect transitions [17], so their n value are both 2. The optical bandgaps of TiO_2 and B were calculated to be 2.87 and 2.22 eV, respectively (Fig. 9b). The bandgap value of TiO_2 is lower than the common 3.2 eV [8,9], which may be caused by the impurity energy level caused by defect state. While the E_g of the B sample lies in the range of 1.55–2.48 eV [17], mainly

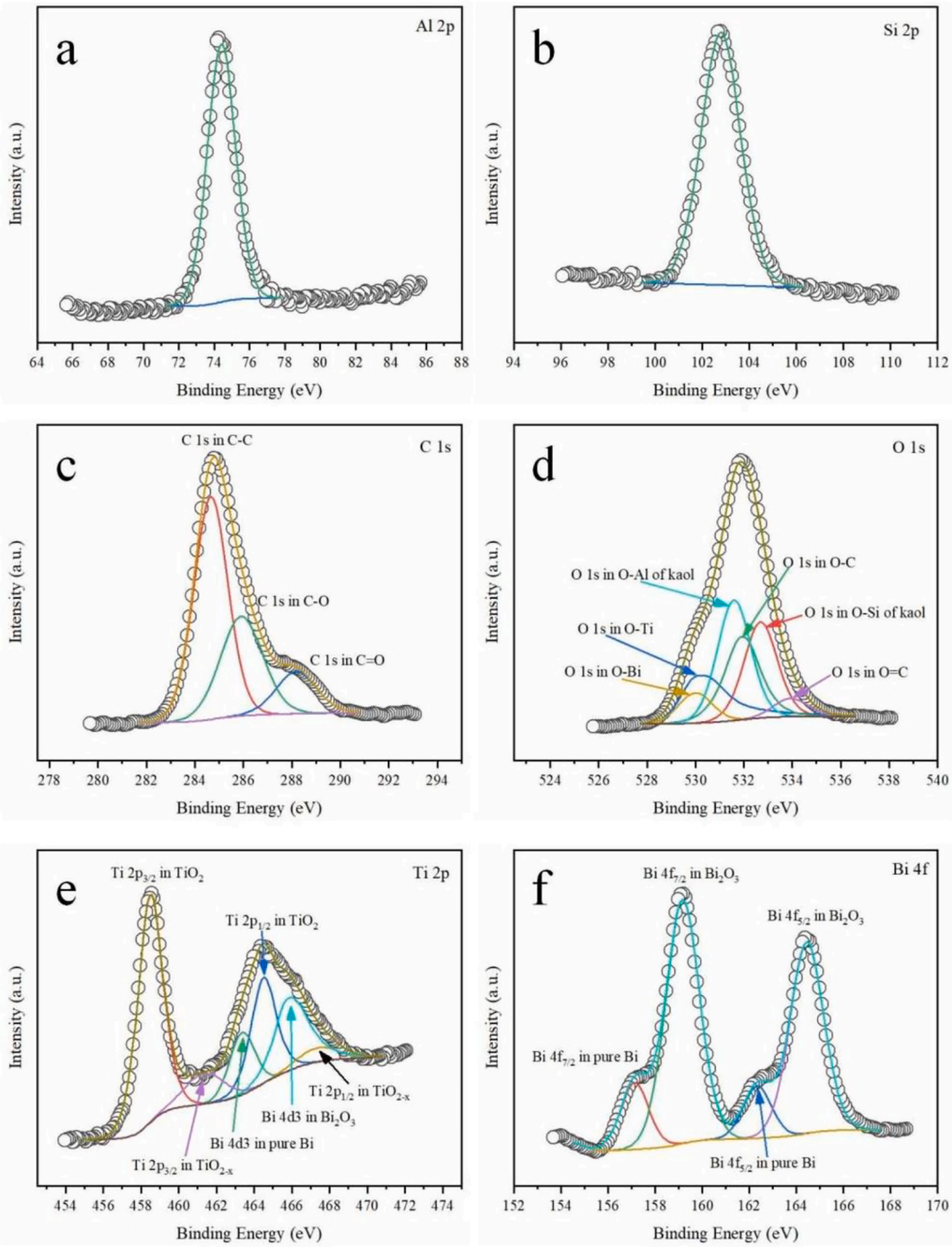

Fig. 7. High-resolution XPS peaks and the best deconvolution to individual components of each element in 1.2KTB sample.

resulting from the contribution of amorphous Bi_xO_y. For the KTB samples, the light absorption significantly increases compared with these samples without B, and the intensity of spectrum increases with B content, reflecting that the addition of B is the main reason for the enhanced light absorption of composites.

3.7. Photocatalytic tests

The photocatalytic performance of the materials was evaluated by degrading MO under irradiation with a low intensity xenon lamp. The photocatalytic results are shown in Fig. 8. In the blank solution, the MO concentration hardly decreased with time (Fig. 8a). Kaolinite showed weak photocatalytic activity, mainly led by trace natural impurities. After TiO_2 was loaded on kaolinite, the formed KT composite showed the improved photocatalytic performance. The photocatalytic effect of KT within 3 h was about one third of that of pure TiO_2 reference. However, KT contains only 11% TiO_2 (according to ICP-OES results in Table S2), suggesting more active TiO_2 in KT than pure TiO_2, so kaolinite substrate should play an important role in enhancing the photocatalytic effect of TiO_2. Sample B had some photocatalytic activity, mainly because the surface Bi_xO_y shell could generate photogenerated carriers with reducing and oxidizing ability when being exposed to simulated sunlight. This result is consistent with an earlier study by Liu et al. [65]. When sample B was compounded with TiO_2 (TB), the photocatalytic effect was improved to a certain extent compared to B, mainly due to the band matching of Bi_xO_y and TiO_2, and this will be discussed further

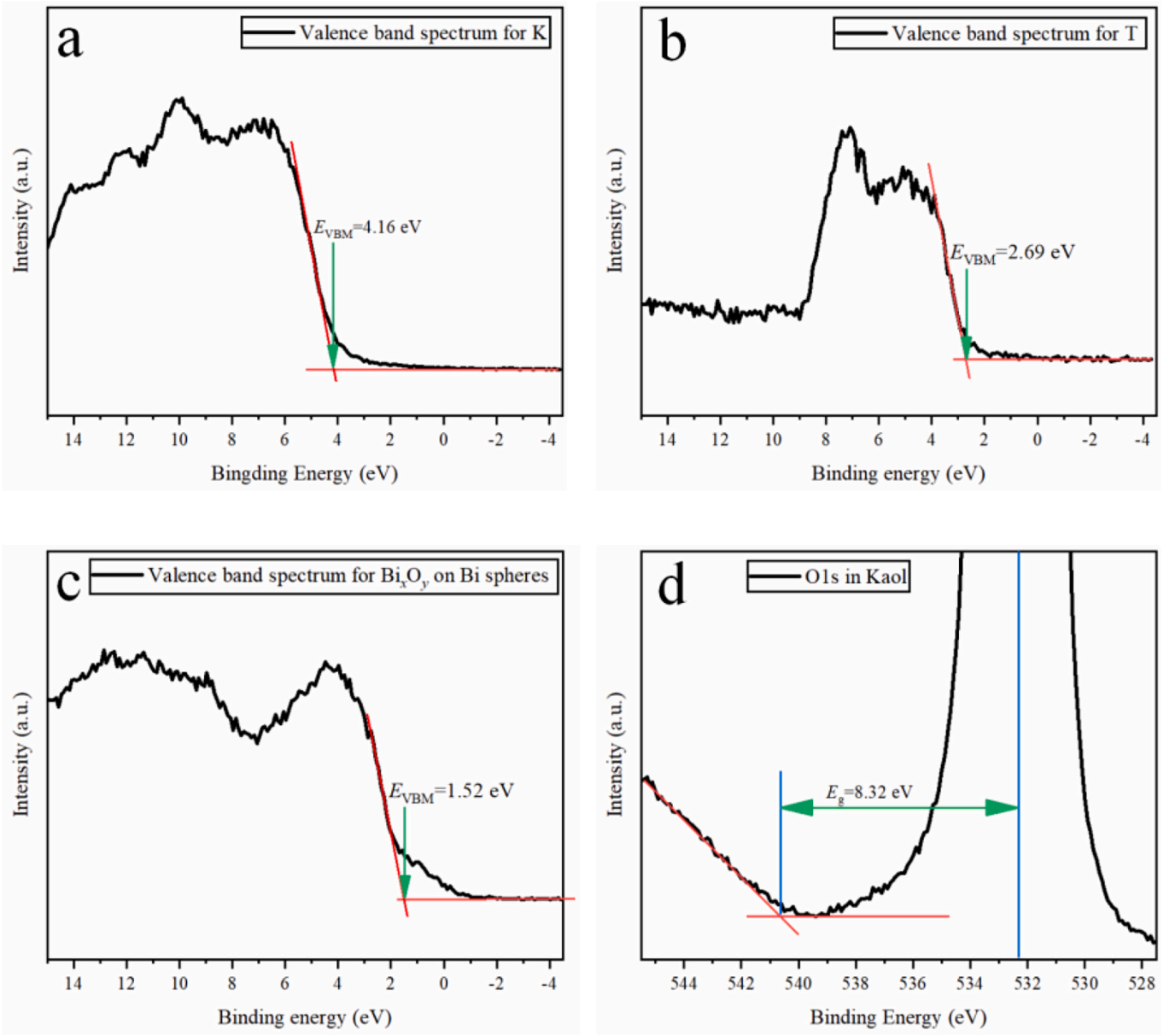

Fig. 8. (a-c) The valence band spectra of K, T and B samples; (d) the energy loss spectra of O in kaolinite.

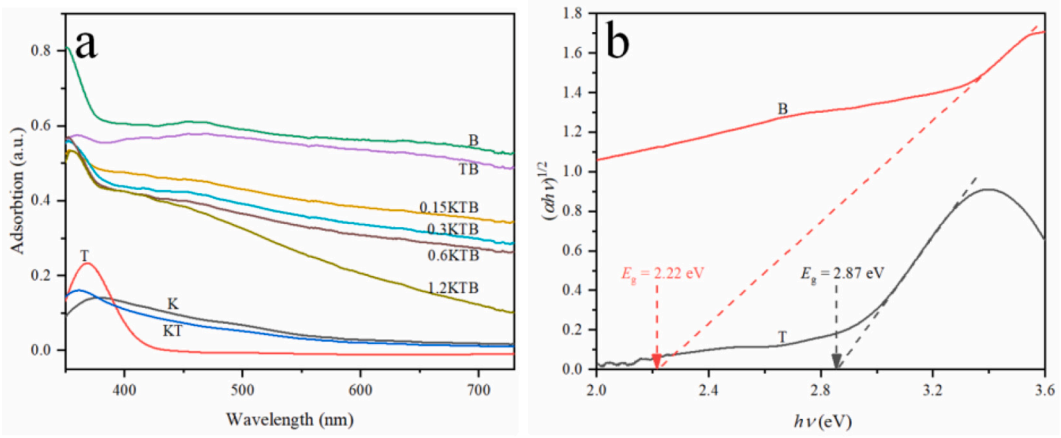

Fig. 9. (a) Diffuse reflection absorption spectrum of samples; (b) Tauc plots for sample T and B.

later. When TiO_2 and B samples were simultaneously loaded on the surface of kaolinite (KTB), the photocatalytic degradation rate of MO was greatly improved, which was significantly better than TiO_2, B, KT and TB samples, and with the increase of KT addition, the performance of the samples gradually improved. When the amount of KT added is 0.6 g (0.6KTB), the performance of the sample tends to be stable and when KT added is 1.2 g (1.2KTB), the performance of the sample reaches the highest activity in the current ratio range of KT to B. Among KTB samples, the performance of 0.15KTB sample is relatively low, which may be because more B reduces the number of T active sites on the surface of kaolinite. With the decrease of B, the shielding effect also decreases, so the performance of the complex increase gradually. When B is reduced to a certain extent, the number of heterostructure between T and B can be reduced too much, which will cancel out the improving effect brought by the increase of T active sites, so the performance will no longer increase significantly.

It is noted that before light on, the dark reaction was carried out for 1 h and the results show that the MO adsorption-desorption balance was achieved for all samples in 1 h (Fig. S8). The MO adsorption capacity of samples was weak, and the difference among equilibrium concentrations for samples was not too much after dark adsorption. When normalizing MO concentration after dark adsorption, the order of photocatalytic efficiency (Fig. S9b) is similar to that when normalizing MO concentration before dark adsorption (Fig. S9a). Thus, the pre-adsorption does not affect the order of the photocatalytic efficiency of the samples significantly.

The total organic carbon (TOC) results of four representative samples (1.2KTB, KT, T and K) have been supplemented to further confirm the occurrence of photocatalytic reaction. The TOC value of initial MO solution is 21.18 μg/kg. For 1.2KTB, the TOC values of MO solution after dark adsorption and after photocatalysis are 20.22 and 12.44 μg/kg, respectively. Such obvious decrease of the TOC value confirms the photodegradation removal of MO, at least to a certain extent. 1.2KTB produced a TOC reduction of 38.5%, while KT, T and K led to TOC reductions of 7.72%, 20.95% and 2.75%, respectively (Table S1).

The degradation kinetic curves were fitted with zero-order equation and pseudo-first-order equation, respectively, the rate constant histograms obtained further intuitively demonstrated the above performance differences. (Fig. 10 and S9). According to the fitting coefficients of determination (COD) (Table S2), the degradation kinetics of MO by KTB composite is more in line with the zero-order reaction, indicating that the photocatalytic process is mainly controlled by the Langmuir–Hinshelwood (L-H) mechanism [79,80], as well as these of B, KT and TB. For K and T, the fitting CODs obtained by using zero-order

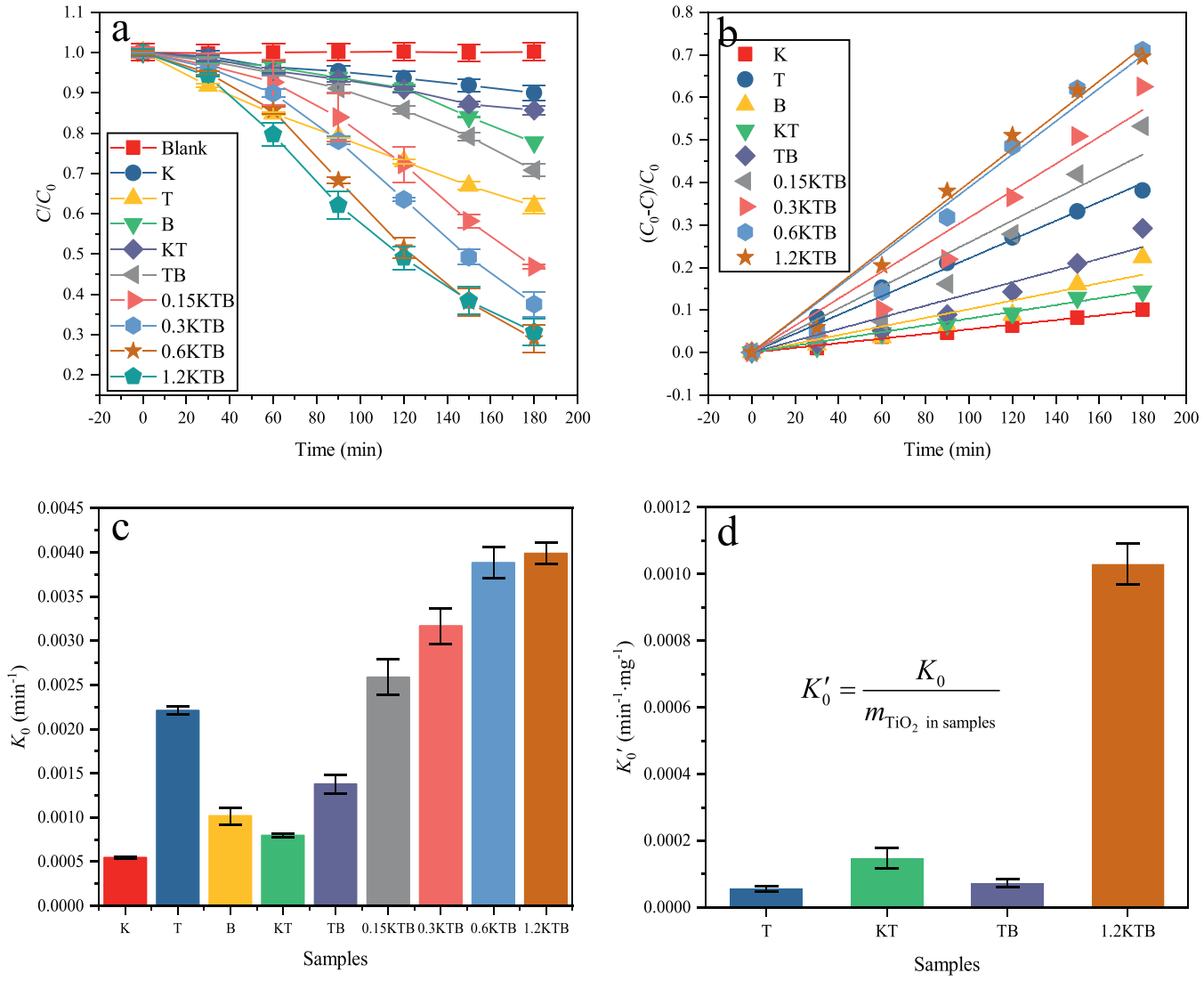

Fig. 10. Photocatalytic curves of samples. (a) Degradation kinetic curves; (b) Zero-order fit; (c) Rate constants for the different samples under study ; (d) Rate constants for typical samples based on the contained TiO_2 mass.

equation and using pseudo-first-order equation are very close, indicating that the L-H mechanism and the Eley–Rideal mechanism might play the similar role for K and T [79,80]. The reason can be that for K substrate without loading photocatalyst, the MO molecules dispersed in solution were directly degraded by ultraviolet energy in light; yet for pure nano TiO_2, many active sites could contact to the reactive species in surrounding solvent. So, the photocatalytic reaction for K and T did not belong to the surface reactions between adsorbed MO and captured active species. Compared with pure T, the rate constants of KTB samples are increased by 1.16–1.79 times; compared with B samples, the rate constants of KTB are increased by 2.49–3.87 times.

In the photodegradation experiments, the total mass of each sample used is the same, but the content of the main catalytic component in the sample is different, which determines the efficiency/cost ratio of each material. Based on the testing results of ICP-OES (Table S3), the reaction rate constant K_0' based on the amount of TiO_2 in the sample is calculated by formula (1) as:

$$K_0^{'} = \frac{K_0}{m_{TiO_2}} \quad (1)$$

where K_0 is the zero-order rate constant obtained by fitting the degradation kinetic curve (corresponding to 40 mg of sample added into 40 mL of MO solution), and m_{TiO2} is the mass of TiO_2 contained in the sample.

According to the calculation result of K', the photodegradation constants based on the TiO_2 mass unit in KT and TB are 2.63 and 1.29 times that of pure TiO_2, indicating that TiO_2 in KT and TB indeed has better catalytic activity than pure TiO_2 (Fig. 10d). The photodegradation constant of TiO_2 in the most typical 1.2KTB sample is even 18.39 times higher than that of pure TiO_2, which further proves the synergistic effect of kaolinite substrate and Bi sphere on the photocatalytic reaction. This result is of great significance for the practical application of the catalyst, because the content of TiO_2 in 1.2KTB is only 9.38%, the content of Bi is only 11.12%, and most of the composite is kaolinite, such composition significantly reduces the cost of catalyst materials.

3.8. Photogenerated carrier separation and transfer analysis

In addition to the light absorption capacity, the separation and transfer efficiency of photogenerated carriers also have an important influence on the final photocatalytic performance of the samples. Photoluminescence spectroscopy (PL) is often used to check the recombination of photogenerated carriers. Generally, the lower the PL peak intensity, the less the recombination of photogenerated carriers, which is more beneficial to the improvement of the photocatalytic performance

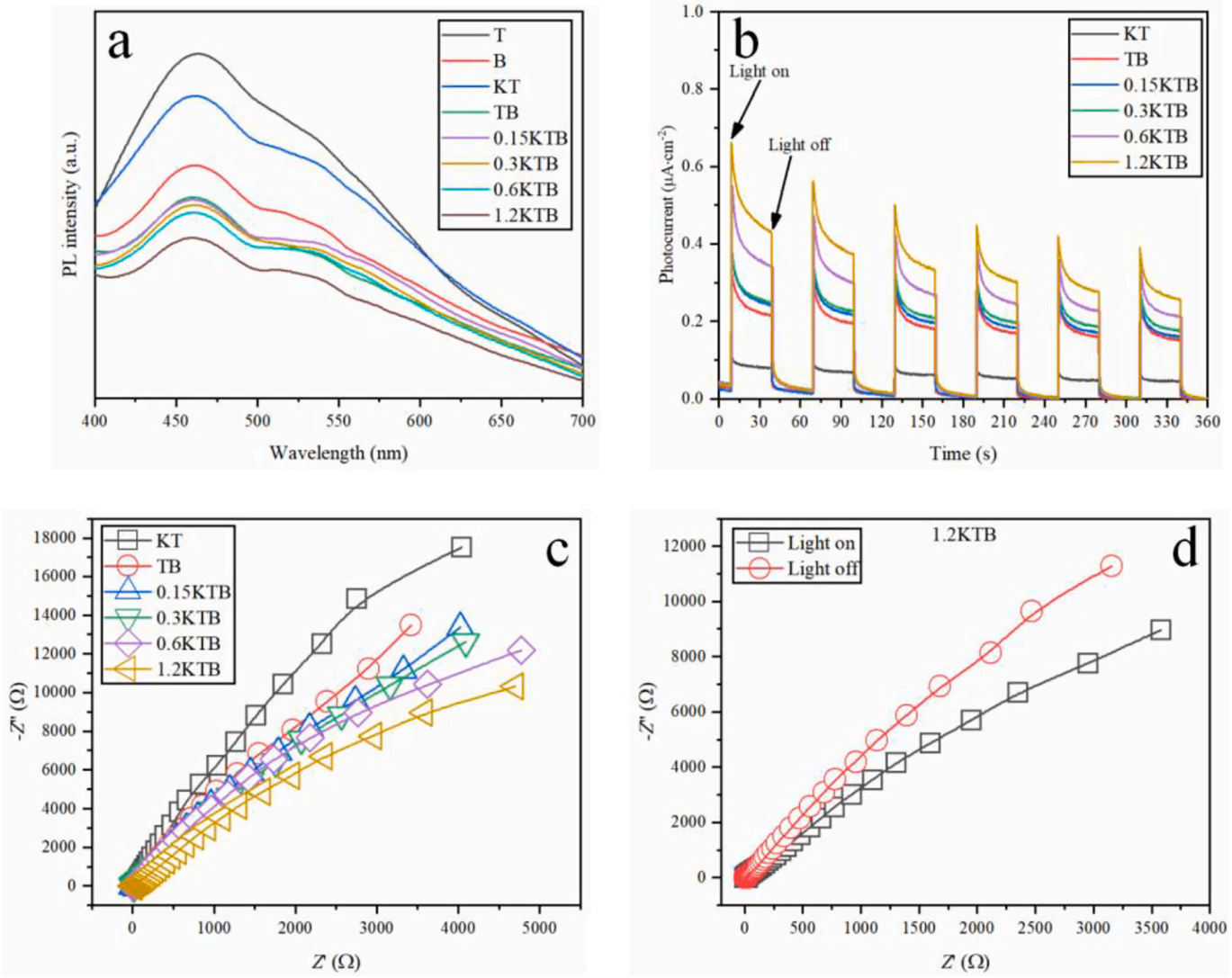

Fig. 11. Characterization of photogenerated charge carrier separation and transfer of samples. (a) Static PL ; (b) photocurrent response plots ; (c) Nyquist plots under light-on condition; (d) Nyquist plots of typical 1.2KTB under light-on and off conditions.

of the sample. Fig. 11a shows the static PL spectra of samples. TiO_2 has a high PL intensity mainly due to its high photogenerated carrier recombination rate. The PL intensity of the KT composite decreased, probably because the improved dispersion of TiO_2 particles reduced the recombination of photogenerated carrier in TiO_2. The PL intensity of sample B is also high, caused by its narrow bandgap, but lower than that of T and KT, probably because the metallic Bi core provides a photogenerated electron container, thus facilitating photogenerated charge separation to some extent. TB has lower PL intensity than pure T and B, suggesting that their band matching is beneficial for the separation of photogenerated carriers. Relative to TB, the PL intensity of KTB continued to decrease, mainly because both the T and B dispersions increased (Fig. 3), reducing the carrier recombination in each; meanwhile, T and B were still in effective contact (Fig. 4), ensuring the suitable matching of their energy band. Fig. 11b shows the response results of the photocurrent over time for a series of consecutive light on and off cycles. It shows a similar trend to the PL spectrum, indicating that KTB produces more extractable charge carriers. In addition, it is found that the samples containing Bi have obvious "tailing" after the light radiation was turned off, which indicates that the addition of B spheres is indeed beneficial to prolong the lifetime of photogenerated carriers, thereby promoting the redox reaction on the catalyst surface.

Electrical impedance spectroscopy (EIS) is an important tool for studying electrode transfer dynamics and surface phenomena. EIS is often represented in photocatalysis as the Nyquist plot. The Nyquist plots of each sample under illumination are shown in Fig. 11. Each plot is arc-shaped, so the surface charge transfer is the reaction rate-determining step. The relative size of the arc radius corresponds to the size of the charge transfer resistance at the electrode interface and the separation efficiency of the photogenerated electron-hole pair. Compared with the KT sample, TB and KTB containing B have smaller arc radii, which further proves that the combination of B spheres with TiO_2 changes the spatial distribution of charges in the samples, thereby reducing the interfacial transport resistance. Within the experimental range, the electrical impedance of the KTB composite decreases gradually with the increase of KT/B ratio, which is consistent with the photocatalytic trend, mainly because agglomeration easily occurs when the content of B spheres is high (Fig. 3e-h), which in turn increases the recombination of photogenerated carriers among B spheres. For 1.2KTB, all B spheres are almost isolated, so the agglomeration effect is minimized; and more KT composite will increase the probability of TiO_2 contacting species in solution, so the photogenerated carriers can be quickly transferred, and the EIS radius is the smallest. Fig. 11d further shows the comparison of the impedance spectrum of 1.2KTB in the dark and after illumination. It can be seen that the arc radius of EIS under illumination is significantly smaller than that under non-illumination, mainly because the carrier concentration in the catalyst increases under illumination, resulting in a decrease in the resistance value of the space charge layer of the sample.

4. Discussion on the enhancement mechanism of photocatalytic performance

4.1. Energy band matching

4.1.1. Determination of energy band position

The bandgap energies of K, TiO_2, and B in the KTB composite, as well as the distance from the Fermi level to the VBM have been obtained through DRS and XPS measurements. However, to determine the mutual matching of their energy levels, it is also necessary to determine their Fermi level positions. The equilibrium condition of a semiconductor in the electrolyte is that the Fermi level at the semiconductor interface is equal to the energy level of the redox potential in the solution, and this can be achieved by the change of carrier distribution to generate the space charge region, leading to the energy band bending at the interface. The energy level of the solution redox potential can be artificially changed by adjusting the potential applied. When it is equal to the internal Fermi level of the semiconductor, no energy band bending will occur. Therefore, the energy level of the solution redox potential corresponds to the Fermi level of the semiconductor in this state.

According to the Mott-Schottky (M-S) equation, the relationship between the capacitance of space charge layer (C_{sc}) and the polarization potential on semiconductor (E_{appl}) can be described in the eq. (2):

$$\frac{1}{C_{SC}^2} = \frac{2}{\varepsilon\varepsilon_0 q N_D}\left(E_{appl} - E_f - \frac{kT}{q}\right) \quad (2)$$

Where ε is the dielectric constant of the semiconductor, ε_0 is the vacuum dielectric constant, q is the electronic charge, N_D is the number of donors, k is Boltzmann's constant and T is the absolute temperature. The curve between $(1/C_{SC})^2$ and polarization potential E_{appl} in the above equation can be obtained by electrochemical measurement. The intercept of the straight part is $(E_f + kT/q)$. As kT/q at room temperature is very small and can be ignored, the intercept represents the flat band potential relative to the reference electrode. When the Ag/AgCl reference electrode is used, the flat band potential can be converted to the value relative to normal hydrogen potential (NHE) by adding 0.197. Because the difference between the redox couple potentials of the solution is equal to that between energy levels, the flat-band potential with respect to NHE (in V) can be written as the energy level with respect to NHE (in eV), that is, the Fermi level with respect to NHE. The reader may refer to some excellent reviews on semiconductor electrochemistry for a more detailed background [81,82].

Here, the E_{flat} of the three components in the KTB composite were determined as shown in Fig. 12. It can be seen that the M-S curve of each sample shows an inverted S shape, and the slope of the straight line part is positive, which are typical *n*-type semiconductors. This result is consistent with that of TiO_2 and amorphous bismuth oxide in the literature [17]. The straight line part of the M-S curve intersects the *x*-axis at −0.24 (T), +0.19 (B) and − 0.10 (K) V (vs normal hydrogen potential, NHE), corresponding to the Fermi levels in the flat band state with the same values and eV unites. Combined with the valence band spectrum data and the DRS bandgap energy data, the positions of VBM and CBM of each component in composite can be further determined, and then the energy band matching of the photo responsive semiconductors can be obtained.

According to the XPS results, the bandgap energy of kaolinite is 8.32 eV, and the distance between the Fermi level and the VBM is 4.16 eV, so the Fermi level is just in the middle of the gap. Based on the M-S result, the position of the Fermi level is obtained at −0.10 eV (vs. NHE), so the positions of CBM and VBM of kaolinite can be obtained at −4.26 and 4.06 eV (vs. NHE). Although CBM and VBM have good reduction and oxidation potentials, the gap between CBM and VBM is too wide, and it is difficult for common light sources to excite valence band electrons, so

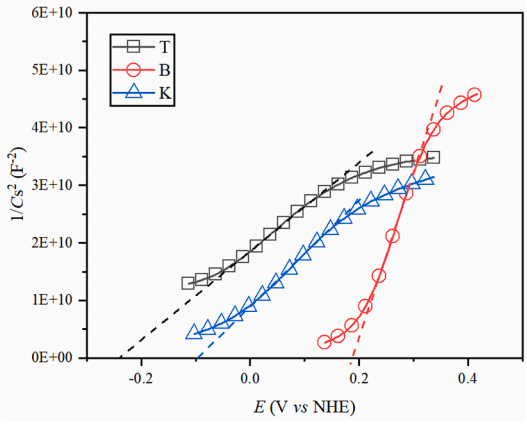

Fig. 12. Mott-Schottky plots of sample T, B and K.

kaolinite is photocatalytic inert. The bandgap width of defective TiO_2 is 2.87 eV, and the distance between the Fermi level and the VBM is 2.69 eV, so the distance between the Fermi level and the CBM is 0.18 eV, which is a typical *n*-type semiconductor feature; moreover, according to the Fermi energy level position (−0.24 eV, vs. NHE), the positions of CBM and VBM can be determined at −0.42 eV and 2.45 eV (vs. NHE), which are more negative than the superoxide ion generation potential and more positive than the hydroxyl radical generation potential, respectively, so the generation conditions of $\cdot O_2^-$ and ·OH are thermodynamically satisfied. The outer surface of sample B is amorphous bismuth oxide, so the surface bismuth oxide mainly plays a catalytic role in degradation process. The energy band data obtained in the experiment is mainly the result of the amorphous bismuth oxide Bi_xO_y which should be somewhat influenced by metallic Bi core. The bandgap of B is 2.22 eV, and the distance between the Fermi level and the VBM is 1.52 eV, so the distance between the Fermi level and the CBM is 0.70 eV, and it also has the characteristics of *n*-type semiconductor, which is consistent with the literature [63]. Moreover, according to its Fermi energy level position (0.19 eV, vs. NHE), the positions of CBM and VBM of sample B can be determined are −0.51 and 1.71 eV (vs. NHE), respectively. Compared with the generation potential of superoxide ion and hydroxyl radical, it predicted that the surface Bi_xO_y can form superoxide ion in photocatalysis, but cannot form hydroxyl radical.

Based on these obtained band positions, a schematic diagram of the band energy of the three components in KTB composite can be drawn (Fig. 12). Kaolinite cannot be excited by solar radiation, and its CBM and VBM are far from these of T and B as expected for an insulator solid. Therefore, due to its energy band structure kaolinite is not expected to intervene in the photocatalytic degradation process considered here. According to the SEM image, TiO_2 nanoparticles are dispersed on the surface of kaolinite, while B particles are further supported on KT, and the two semiconductors T and Bi_xO_y are in direct contact. Since the CBM position of Bi_xO_y is higher than that of T, the photogenerated electrons in Bi_xO_y are transferred to the CBM of T under the driving of the potential difference; at the same time, the photogenerated holes in T are transferred to the VBM of B. In this way, the effective separation of photogenerated carriers in B and T is achieved. The photogenerated carriers are collected on the CBM of TiO_2 for reduction reaction, while the photogenerated holes are collected on the VBM of B for the oxidation reaction, that is, the type-II heterojunction is formed [83].

4.1.2. Experimental verification through photocatalytic capture tests

In order to confirm the operation of the type-II scheme proposed above for the T-B heterojunction, different trapping agents were added to the reaction system to detect the reactive intermediate species during the degradation of MO dye. Among them, IPA was used to trap ·OH, AO was used to quench h^+, and BQ to capture $\cdot O_2^-$. Fig. 14 shows the histograms of the rate constants of each sample of the series in the capture experiment. For TiO_2, the addition of the three scavengers all lead to a certain decrease in the photocatalytic reaction rate, indicating that ·OH, h^+ and $\cdot O_2^-$ are all active species, which exactly corresponds to the CBM and VBM position of TiO_2 in Fig. 13. For sample B, AO and BQ scavengers have obvious effects on the photocatalytic performance, indicating that h^+ and $\cdot O_2^-$ are the main active species, and this is also consistent with the CBM and VBM potentials estimated for B. For TB and KTB, the effect of the capture agent is similar to that of B. Both h^+ and $\cdot O_2^-$ active species play a main role, mainly due to the formation of a type-II heterojunction between T and B, resulting in the reduction potential at the CBM position of TiO_2 and the oxidation potential at the VBM position of B, as shown in Fig. 13.

In addition, it is found that in the capture experiments of Bi-containing samples, the role of photogenerated holes was more obvious than that of superoxide ions. There may be two reasons: one is that the photogenerated holes themselves have strong oxidizing ability and can directly oxidize organic pollutants, while the superoxide ion needs to be converted into other strongly oxidizing intermediate species

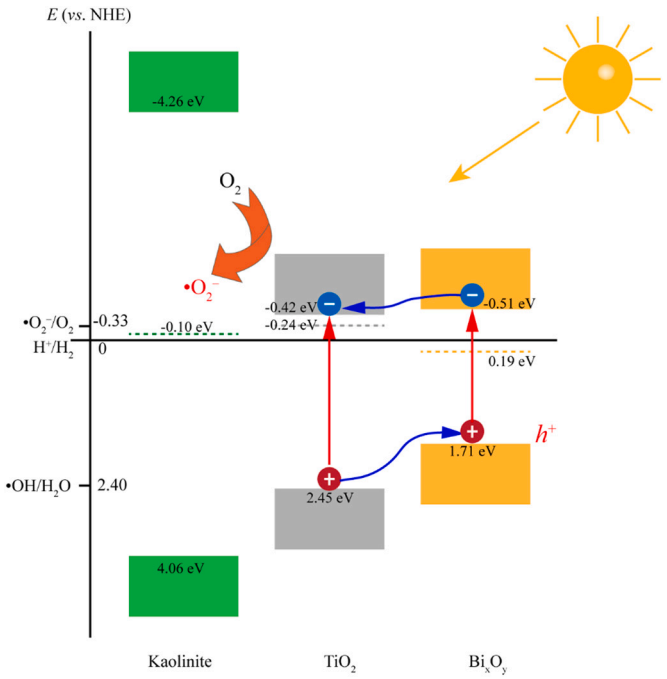

Fig. 13. Energy level diagram of the three components (K, T and B) in the KTB composite.

(such as H_2O_2, ·OH)to degrade organic matter through a complex multistep reaction which requires longer kinetics, so the degradation rate is slower.

$$\cdot O_2^- + H^+ \rightarrow HO_2\cdot \quad (3)$$

$$2HO_2\cdot \rightarrow O_2 + H_2O_2 \quad (4)$$

$$H_2O_2 + \cdot O_2^- \rightarrow H_2O + HO_2\cdot \quad (5)$$

Other aspect to be considered is that the role of the metal Bi core of the B sphere, as an electron buffer, storing a part of the photogenerated electrons. Accordingly, the fraction of the photogenerated electrons on the metallic B core is not easy to be trapped by the quencher in solution, resulting in a decrease in the number of available photogenerated electrons. Therefore, the effect of photogenerated electrons on photocatalytic degradation is weaker than that of photogenerated holes.

4.2. The role of clay substrate

In addition of the proper matching of the T and B energy bands, the good photocatalytic performance of KTB is also due to the role of kaolinite as support. This role is clearly demonstrated by the comparison of the photocatalytic performance of the KTB sample containing kaolinite support and the TB sample without kaolinite substrate in Fig. 10. The promotion of the photocatalytic performance by kaolinite can be attributed to the following two reasons:

4.2.1. Improved TiO_2 dispersion

In the synthesis of KT or KTB composites, kaolinite flakes added to the TTIP precursor solution can serve as a substrate for heterogeneous nucleation of TiO_2, and the growth of TiO_2 attached to the surface of kaolinite effectively avoids the nanoparticle agglomeration. Fig. 15 presents a direct comparison of the TEM image of TiO_2 and KT. It can be seen that the TiO_2 sample is seriously agglomerated, but with the kaolinite substrate, TiO_2 is dispersed into a thin layer on kaolinite surface, which indeed reduces the agglomeration of the TiO_2 particles and exposes more active sites. On the one hand, this distribution reduces the recombination of photogenerated carriers in TiO_2, and on the other

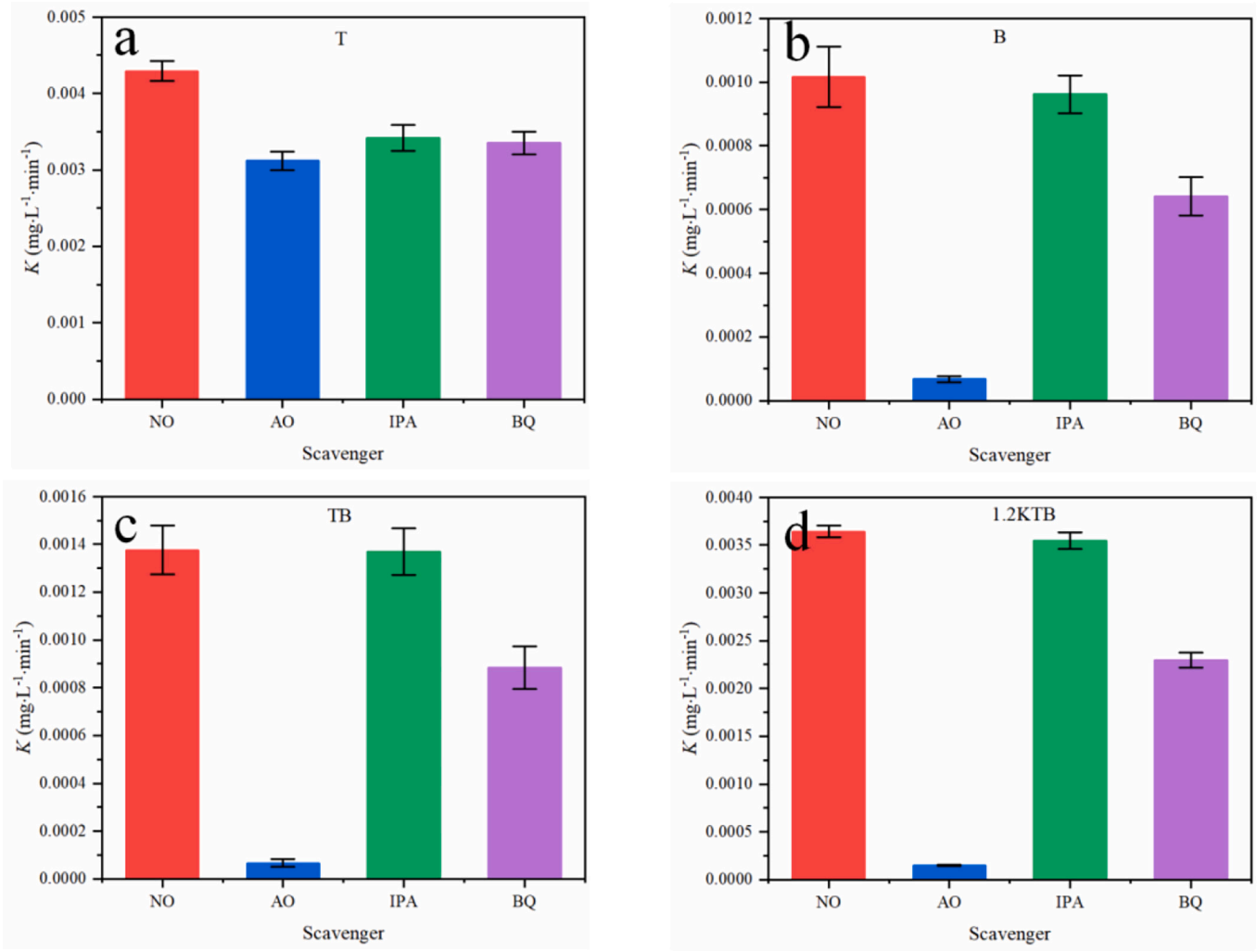

Fig. 14. Rate constants for the series of samples under study in the presence of selective quenchers.

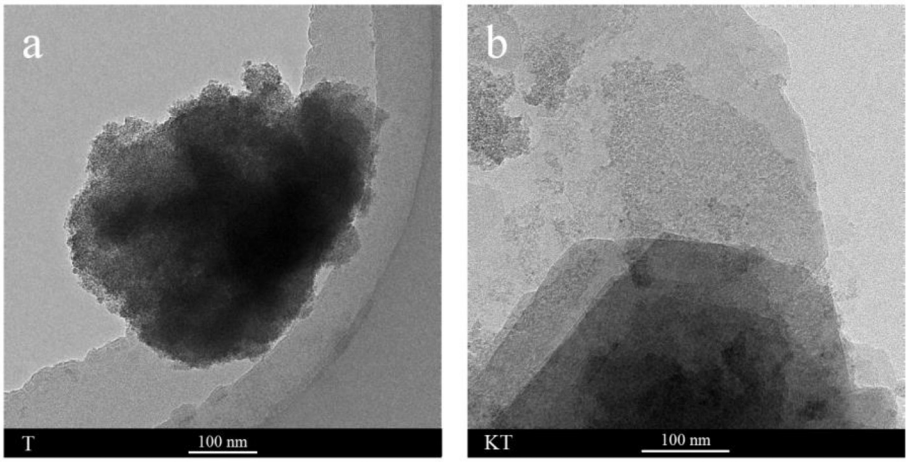

Fig. 15. TEM images of comparing the dispersion of pure TiO_2 (a) and TiO_2 on the surface of kaolinite (b).

hand, it also facilitates the rapid transfer of photogenerated carriers to B spheres supported on the KT surface, or direct redox reactions with other substances in the solution. Therefore, the photocatalytic performance can be effectively improved.

4.2.2. Improved adsorption of oxygen and MO molecules

Oxygen molecules dissolved in water can capture photogenerated electrons on the surface of the catalyst, and these captured electrons are more stable than free electrons, which is beneficial for the photochemical degradation. After oxygen molecules capture electrons, superoxide

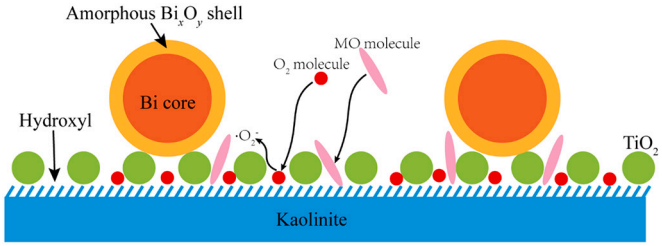

Fig. 16. Schematic role of kaolinite in photocatalytic reaction.

ions with strong oxidizing ability will be formed, or further converted into oxidizing species such as hydrogen peroxide and hydroxyl radicals. Therefore, the number of oxygen molecules adsorbed near the catalyst has an important influence on the photocatalytic ability of the catalyst. Through the simulations of density functional theory (DFT), Jiang et al. found that kaolinite surface hydroxyl groups have a stronger hydrogen bond attraction to oxygen in the presence of water molecules [84], which is consistent with the photocatalytic reaction environment of the aqueous system employed here. In addition, we also found that oxygen molecules in the water system tend to be spontaneously adsorbed on kaolinite surface above the tri-hydroxyl center by the Monte Carlo simulation [45]. All these results indicate that kaolinite can adsorb oxygen molecules in water, increasing the oxygen concentration around the photoresponsive components, thereby increasing the probability of the reaction of TiO_2 and nearby O_2 molecules to generate superoxide ions, facilitating the photocatalytic degradation of MO.

In addition to O_2 molecules, kaolinite also participates by adsorption of MO molecules. Our previous Monte Carlo simulation results show that MO anions are very easily adsorbed on the kaolinite hydroxyl surface, which forms hydrogen bonds through the two sulfonic oxygen atoms and kaolinite surface hydroxyl groups, while the carbon chain of MO and the kaolinite sheet form a certain angle [45]. The results further confirm that the addition of kaolinite can aggregate surrounding MO molecules, thereby increasing the probability of the reaction of photocatalyst holes and MO reaction, again improving photocatalytic degradation efficiency.

Therefore, although kaolinite cannot be excited by the solar radiation and cannot directly affect the photocatalytic performance of the composite in terms of band structure matching, the efficiency of the photoresponsive components and the probability of the catalytic reaction increase, by the effect of K, improving the dispersion of TiO_2 nanoparticles and the adsorption of O_2 and MO molecules, resulting in significantly improved photocatalytic performance of KTB composite (Fig. 16).

5. Conclusions

In this work, a novel kaolinite/TiO_2/core-shell Bi sphere composite photocatalyst has successfully been synthesized by a combined hydrothermal-solvothermal method, which exhibited significantly improved photocatalytic performance for MO degradation under weak power sunlight illumination. Through the characterization of the morphology, structure and properties of the samples with a series of KT/B ratios, the following conclusions are obtained:

(1) In KTB composites, TiO_2 is anatase phase containing defect states, and B component has the core (metal Bi) - shell (amorphous bismuth oxide) structure. TiO_2 shows the morphology of nanoparticles well dispersed on the surface of kaolinite, while B is microspheres distributed on TiO_2 and with the increase of the amount, the aggregation of B spheres increases.

(2) Compared with T and KT, KTB composite shows the significantly improved light absorption in the investigated spectral range which increases with the content of B; the photoluminescence, photoelectric response and EIS properties of the KTB sample are obviously better than those of KT and TB.

(3) Compared with T, B, KT and TB, a photocatalytic performance of KTB composites is greatly improved, the activity increasing with the increase of KT content; when the KT addition is 1.2 g (1.2KTB), the photocatalytic performance of the sample is the highest of the series. The photocatalytic performance in terms of TiO_2 mass unit in 1.2KTB even reaches 18.39, 14.26 and 6.99 times that of TiO_2 in T, TB and KT.

(4) DRS, XPS, M-S data and trapping experiments show that in terms of the promotion of photocatalysis by energy band matching, TiO_2 and bismuth oxide on the surface of B sphere form a typical type-II heterojunction, which promotes the separation of photogenerated electron-hole pairs, while kaolinite cannot be excited by the solar spectrum and cannot significantly affect the photocatalytic performance of the composite through band structure matching.

(5) Kaolinite increases the available TiO_2 active sites by improving the dispersion of TiO_2 nanoparticles, and can promote the reaction between the catalyst and surrounding species through the adsorption of oxygen molecules and MO molecules, thereby achieving a significant improvement in the photocatalytic performance of KTB.

CRediT authorship contribution statement

Chen Li: Methodology, Formal analysis, Writing – original draft. **Li Sun:** Validation, Visualization. **Jinan Niu:** Conceptualization, Writing – review & editing. **Arianit A. Reka:** Writing – review & editing. **Peizhong Feng:** Funding acquisition, Resources. **Hermenegildo Garcia:** Writing – review & editing.

Declaration of Competing Interest

The authors declare that they have no known competing financial interests or personal relationships that could have appeared to influence the work reported in this paper.

Data availability

The data that has been used is confidential.

Acknowledgement

This work is supported by the Fundamental Research Funds for the Central Universities (2019XKQYMS76).

Appendix A. Supplementary data

Supplementary data to this article can be found online at https://doi.org/10.1016/j.catcom.2023.106609.

References

[1] Q. Guo, C. Zhou, Z. Ma, X. Yang, Fundamentals of TiO_2 photocatalysis: concepts, mechanisms, and challenges, Adv. Mater. 31 (2019), e1901997.
[2] J. Wang, R.T. Guo, Z.X. Bi, X. Chen, X. Hu, W.G. Pan, A review on TiO_{2-x}-based materials for photocatalytic CO_2 reduction, Nanoscale 14 (2022) 11512–11528.
[3] M. Hadei, A. Mesdaghinia, R. Nabizadeh, A.H. Mahvi, S. Rabbani, K. Naddafi, A comprehensive systematic review of photocatalytic degradation of pesticides using nano TiO_2, Environ. Sci. Pollut. R. 28 (2021) 13055–13071.
[4] A. Hezam, Q.A. Drmosh, D. Ponnamma, M.A. Bajiri, M. Qamar, K. Namratha, M. Zare, M.B. Nayan, S.A. Onaizi, K. Byrappa, Strategies to enhance ZnO photocatalyst's performance for water treatment: a comprehensive review, Chem. Rec. 22 (2022), e202100299.
[5] C.M. Oral, M. Ussia, M. Pumera, Hybrid enzymatic/photocatalytic degradation of antibiotics via morphologically programmable light-driven ZnO microrobots, Small 18 (2022), e2202600.
[6] T. Du, Y. Zhang, Y. Chao, Y. An, C. Meng, In situ growth of hierarchical phase junction CdS on a H-mordenite zeolite for enhanced photocatalytic properties, Dalton T 51 (2022) 12975–12985.
[7] Z. Tai, G. Sun, T. Wang, Z. Fang, X. Hou, F. Li, Y. Qiu, Q. Ye, L. Jia, H. Wang, Defected tungsten disulfide decorated CdS nanorods with covalent heterointerfaces for boosted photocatalytic H2 generation, J. Colloid Interface Sci. 628 (2022) 252–260.

[8] P.V. Kamat, TiO_2 nanostructures: recent physical chemistry advances, J. Phys. Chem. C 116 (2012) 11849–11851.
[9] V. Etacheri, C. Di Valentin, J. Schneider, D. Bahnemann, S.C. Pillai, Visible-light activation of TiO_2 photocatalysts: advances in theory and experiments, J Photochem Photobiol C: Photochem Rev 25 (2015) 1–29.
[10] J. Kosco, S. Gonzalez-Carrero, C.T. Howells, T. Fei, Y. Dong, R. Sougrat, G. T. Harrison, Y. Firdaus, R. Sheelamanthula, B. Purushothaman, F. Moruzzi, W. Xu, L. Zhao, A. Basu, S. De Wolf, T.D. Anthopoulos, J.R. Durrant, I. McCulloch, Generation of long-lived charges in organic semiconductor heterojunction nanoparticles for efficient photocatalytic hydrogen evolution, Nat. Energy 7 (2022) 340–351.
[11] S. Bai, J. Jiang, Q. Zhang, Y. Xiong, Steering charge kinetics in photocatalysis: intersection of materials syntheses, characterization techniques and theoretical simulations, Chem. Soc. Rev. 44 (2015) 2893–2939.
[12] A. Kumar, P. Choudhary, A. Kumar, P.H.C. Camargo, V. Krishnan, Recent advances in plasmonic photocatalysis based on TiO_2 and noble metal nanoparticles for energy conversion, environmental remediation, and organic synthesis, Small 18 (2022), e2101638.
[13] N. Chakinala, P.R. Gogate, A.G. Chakinala, Highly efficient bi-metallic bismuth-silver doped TiO_2 photocatalyst for dye degradation, Korean J. Chem. Eng. 38 (2021) 2468–2478.
[14] W. Feng, J. Li, Z. Lei, Y. Liu, Y. Shen, Z. Chen, The improved photocatalytic activity of $CaWO_4$ nanorods by loading Bi on the surface, J. Mater. Sci. Mater. Electron. 30 (2019) 16049–16055.
[15] L. Zhang, C. Yang, K. Lv, Y. Lu, Q. Li, X. Wu, Y. Li, X. Li, J. Fan, M. Li, SPR effect of bismuth enhanced visible photoreactivity of Bi_2WO_6 for NO abatement, Chin. J. Catal. 40 (2019) 755–764.
[16] R. Sasikala, B. Subash, Synthesis, characterization of Bi/ZnO and its photoactivity towards TB, AR 27 & RR 120 degradation under UV-A light, Optik 178 (2019) 1079–1089.
[17] L. Leontie, M. Caraman, M. Delibaş, G. Rusu, Optical properties of bismuth trioxide thin films, Mater. Res. Bull. 36 (2001) 1629–1637.
[18] A. Hameed, V. Gombac, T. Montini, L. Felisari, P. Fornasiero, Photocatalytic activity of zinc modified Bi_2O_3, Chem. Phys. Lett. 483 (2009) 254–261.
[19] A.H. Zahid, Q. Han, A review on the preparation, microstructure, and photocatalytic performance of Bi_2O_3 in polymorphs, Nanoscale 13 (2021) 17687–17724.
[20] S. Xia, G. Zhang, Z. Gao, Y. Meng, B. Xie, H. Lu, Z. Ni, 3D hollow Bi_2O_3@CoAl-LDHs direct Z-scheme heterostructure for visible-light-driven photocatalytic ammonia synthesis, J. Colloid Interface Sci. 604 (2021) 798–809.
[21] H. Zhang, L.C. Nengzi, Z. Wang, X. Zhang, B. Li, X. Cheng, Construction of Bi_2O_3/CuNiFe LDHs composite and its enhanced photocatalytic degradation of lomefloxacin with persulfate under simulated sunlight, J. Hazard. Mater. 383 (2020), 121236.
[22] W. Liu, Z. Li, Q. Kang, L. Wen, Efficient photocatalytic degradation of doxycycline by coupling alpha-Bi_2O_3/g-C_3N_4 composite and H_2O_2 under visible light, Environ. Res. 197 (2021), 110925.
[23] Z. Khazaee, A.R. Mahjoub, A.H.C. Khavar, V. Srivastava, M. Sillanpaa, Sub-level engineering strategy of nitrogen-induced Bi_2O_3/g-C_3N_4: a versatile photocatalyst for oxidation and reduction, Environ. Sci. Pollut. R. 28 (2021) 50747–50766.
[24] Y. Bi, Y. Yang, X.L. Shi, L. Feng, X. Hou, X. Ye, L. Zhang, G. Suo, J. Chen, Z.G. Chen, Bi_2O_3/$BiVO_4$@graphene oxide van der Waals heterostructures with enhanced photocatalytic activity toward oxygen generation, J. Colloid Interface Sci. 593 (2021) 196–203.
[25] J. Zhou, F. Duo, C. Wang, L. Chu, M. Zhang, D. Yan, Robust photocatalytic activity of two-dimensional h-BN/Bi_2O_3 heterostructure quantum sheets, RSC Adv. 12 (2022) 13535–13547.
[26] H. Baniamerian, M. Teimoori, M. Saberi, Fe_2O_3/TiO_2/activated carbon nanocomposite with synergistic effect of adsorption and photocatalysis, Chem. Eng. Technol. 44 (2021) 130–139.
[27] R.Q. Yu, X.C. Yu, J.Y. Fu, Y.X. Zhang, Y.F. Liu, Y.Q. Zhang, S.N. Wu, Removal of ammonia nitrogen in aquaculture wastewater by composite photocatalyst TiO_2/carbon fibre, Water Environ. J. 35 (2021) 962–970.
[28] C. Bobirica, L. Bobirica, M. Rapa, E. Matei, A.M. Predescu, C. Orbeci, Photocatalytic degradation of ampicillin using PLA/TiO_2 hybrid nanofibers coated on different types of fiberglass, Water-Sui 12 (2020).
[29] A. Bjelajac, R. Petrovic, J. Vujancevic, K. Veltruska, V. Matolin, Z. Siketic, G. Provatas, M. Jaksic, G.E. Stan, G. Socol, I.N. Mihailescu, D. Janackovic, Sn-doped TiO_2 nanotubular thin film for photocatalytic degradation of methyl orange dye, J. Phys. Chem. Solids 147 (2020).
[30] G.Q. Guo, H.Y. Guo, F. Wang, L.J. France, W.X. Yang, Z.H. Mei, Y.H. Yu, Dye-sensitized TiO_2@SBA-15 composites: preparation and their application in photocatalytic desulfurization, Green Energy Environ. 5 (2020) 114–120.
[31] J.L. Jiang, C.S. Duanmu, Y. Yang, X. Gu, J. Chen, Synthesis and characterization of high siliceous ZSM-5 zeolite from acid-treated palygorskite, Powder Technol. 251 (2014) 9–14.
[32] J.L. Jiang, Y. Xu, C.S. Duanmu, X. Gu, J. Chen, Preparation and catalytic properties of sulfonated carbon-palygorskite solid acid catalyst, Appl. Clay Sci. 95 (2014) 260–264.
[33] D.Y. Tan, Y. Li, Z. Zhang, S.Y. Sun, H.J. Sun, B.W. Li, Selective loading and prolonged release of 5-fluorouracil in the nanoconfined interlayer space of montmorillonite, J. Nanosci. Nanotechnol. 21 (2021) 781–787.
[34] D. Tan, P. Yuan, F. Dong, H. He, S. Sun, Z. Liu, Selective loading of 5-fluorouracil in the interlayer space of methoxy-modified kaolinite for controlled release, Appl. Clay Sci. 159 (2018) 102–106.
[35] X.F. Hao, H.J. Hu, Z. Li, L.M. Wu, X.Q. Liu, Y.N. Zhang, Adsorption properties of modified clinoptilolite for methane and nitrogen, Materials 11 (2018) 2024.
[36] J.N. Niu, Y.H. Qiang, X. Li, Z.S. Liu, S.H. Zhang, P.Z. Feng, X.M. Ou, Morphology and orientation of curling of kaolinite layer in hydrate, Appl. Clay Sci. 101 (2014) 215–222.
[37] H. Islam, M. Susan, A.B. Imran, Effects of plasticizers and clays on the physical, chemical, mechanical, thermal, and morphological properties of potato starch-based nanocomposite films, ACS Omega 5 (2020) 17543–17552.
[38] A.P. Vasilev, T.S. Struchkova, L.A. Nikiforov, A.A. Okhlopkova, P.N. Grakovich, E. L. Shim, J.H. Cho, Mechanical and tribological properties of polytetrafluoroethylene composites with carbon fiber and layered silicate fillers, Molecules 24 (2019) 224.
[39] Q.H. Zhao, L.J. Fu, D.H. Jiang, J. Ouyang, Y.H. Hu, H.M. Yang, Y.F. Xi, Nanoclay-modulated oxygen vacancies of metal oxide, Commun. Chem. 2 (2019) 1–10.
[40] Q.H. Zhao, L.J. Fu, D.H. Jiang, Y.F. Xi, H.M. Yang, A nanoclay-induced defective g-C_3N_4 photocatalyst for highly efficient catalytic reactions, Chem. Commun. 54 (2018) 8249–8252.
[41] H.L. Xu, J.H. Liu, P. Chen, G. Shao, B.B. Fan, H.L. Wang, D.L. Chen, H.X. Lu, R. Zhang, Preparation of magnetic kaolinite nanotubes for the removal of methylene blue from aqueous solution, J. Inorg. Organomet. Polym. Mater. 28 (2018) 790–799.
[42] H.F. Cheng, Y. Zhou, Y.P. Feng, W.X. Geng, Q.F. Liu, W. Guo, L. Jiang, Electrokinetic energy conversion in self-assembled 2D nanofluidic channels with Janus nanobuilding blocks, Adv. Mater. 29 (2017) 1700177.
[43] Y. Zhou, A.M. LaChance, A.T. Smith, H.F. Cheng, Q.F. Liu, L.Y. Sun, Strategic design of clay-based multifunctional materials: from natural minerals to nanostructured membranes, Adv. Funct. Mater. 29 (2019) 1807611.
[44] A.C. Wu, D.X. Wang, C. Wei, X.D. Zhang, Z.S. Liu, P.Z. Feng, X.M. Ou, Y.H. Qiang, H. Garcia, J.N. Niu, A comparative photocatalytic study of TiO_2 loaded on three natural clays with different morphologies, Appl. Clay Sci. 183 (2019), 105352.
[45] R.Y. Chen, D.X. Lai, D.X. Wang, J.N. Niu, J. He, P.Z. Feng, H. Garcia, Enhanced photocatalytic activity of kaolinite-TiO_2-graphene oxide composite with a porous stacking structure, J. Alloys Compd. 889 (2021), 161682.
[46] A.H. Zyoud, T. Zorba, M. Helal, S. Zyoud, N. Qamhiya, A.R. Hajamohideen, S. Zyoud, H.S. Hilal, Direct sunlight-driven degradation of 2-chlorophenol catalyzed by kaolinite-supported ZnO, Int. J. Environ. Sci. Technol. 16 (2019) 6267–6276.
[47] K. Koci, V. Matejka, P. Kovar, Z. Lacny, L. Obalova, Comparison of the pure TiO_2 and kaolinite/TiO_2 composite as catalyst for CO_2 photocatalytic reduction, Catal. Today 161 (2011) 105–109.
[48] H.L. Xu, S.P. Sun, S.Y. Jiang, H.L. Wang, R. Zhang, Q.F. Liu, Effect of pretreatment on microstructure and photocatalytic activity of kaolinite/TiO_2 composite, J. Sol-Gel Sci. Technol. 87 (2018) 676–684.
[49] Y.P. Zhao, Z. Cao, A.A. Zuh, Y.F. Jia, Q.Z. Wang, H.F. Cheng, Synthesis of bismuth oxyiodide/kaolinite composite with enhanced photocatalytic activity, J. Phys. Chem. Solids 161 (2022), 110424.
[50] Y.P. Zhao, Z. Cao, Y. Chen, Y.F. Jia, Q.Z. Wang, H.F. Cheng, Heterostructure coal-bearing strata kaolinite/$MnFe_2O_4$ composite for activation of peroxydisulfate to efficiently degrade chlortetracycline hydrochloride, Coll. Surf. A 643 (2022), 128789.
[51] X.B. Dong, B.X. Ren, Z.M. Sun, C.Q. Li, X.W. Zhang, M.H. Kong, S.L. Zheng, D. D. Dionysiou, Monodispersed $CuFe_2O_4$ nanoparticles anchored on natural kaolinite as highly efficient peroxymonosulfate catalyst for bisphenol a degradation, Appl. Catalysis B-Environ. 253 (2019) 206–217.
[52] C.Q. Li, Z.M. Sun, W.Z. Zhang, C.H. Yu, S.L. Zheng, Highly efficient g-C_3N_4/TiO_2/kaolinite composite with novel three-dimensional structure and enhanced visible light responding ability towards ciprofloxacin and *S. aureus*, Appl. Catalysis B-Environ. 220 (2018) 272–282.
[53] C.Q. Li, Z.M. Sun, A.K. Song, X.B. Dong, S.L. Zheng, D.D. Dionysiou, Flowing nitrogen atmosphere induced rich oxygen vacancies overspread the surface of TiO_2/kaolinite composite for enhanced photocatalytic activity within broad radiation spectrum, Appl. Catalysis B-Environ. 236 (2018) 76–87.
[54] X.Y. Li, H.M. Yang, Pd hybridizing ZnO/kaolinite nanocomposites: synthesis, microstructure, and enhanced photocatalytic property, Appl. Clay Sci. 100 (2014) 43–49.
[55] Z. Cao, Q.Z. Wang, H.F. Cheng, Recent advances in kaolinite-based material for photocatalysts, Chin. Chem. Lett. 32 (2021) 2617–2628.
[56] B.X. Zhao, L.M. Liu, H.F. Cheng, Rational design of kaolinite-based photocatalytic materials for environment decontamination, Appl. Clay Sci. 208 (2021), 106098.
[57] C.Q. Li, N.Y. Zhu, S.S. Yang, X.W. He, S.L. Zheng, Z.M. Sun, D.D. Dionysiou, A review of clay based photocatalysts: role of phyllosilicate mineral in interfacial assembly, microstructure control and performance regulation, Chemosphere 273 (2021), 129723.
[58] W.K. Fan, M. Tahir, Structured clay minerals-based nanomaterials for sustainable photo/thermal carbon dioxide conversion to cleaner fuels: a critical review, Sci. Total Environ. 845 (2022), 157206.
[59] E.M. Serwicka, Titania-clay mineral composites for environmental catalysis and photocatalysis, Catalysts 11 (2021) 1087.
[60] M.C. Dlamini, M.S. Maubane-Nkadimeng, J.A. Moma, The use of TiO_2/clay heterostructures in the photocatalytic remediation of water containing organic pollutants: a review, J. Environ. Chem. Eng. 9 (2021), 106546.
[61] A. Raza, R. Rehman, M. Batool, Recent review of titania-clay-based composites emerging as advanced adsorbents and photocatalysts for degradation of dyes over the last decade, Adsorpt. Sci. Technol. 2022 (2022) 3823008.

[62] Y.T. Zou, Y.Z. Hu, Z.W. Shen, L. Yao, D.Y. Tang, S. Zhang, S.Q. Wang, B.W. Hu, G. X. Zhao, X.K. Wang, Application of aluminosilicate clay mineral-based composites in photocatalysis, J. Environ. Sci. 115 (2022) 190–214.
[63] W.K. Jo, T.S. Natarajan, Influence of TiO_2 morphology on the photocatalytic efficiency of direct Z-scheme g-C_3N_4/TiO_2 photocatalysts for isoniazid degradation, Chem. Eng. J. 281 (2015) 549–565.
[64] C. Li, J. Wang, S. Feng, Z. Yang, S. Ding, Low-temperature synthesis of heterogeneous crystalline TiO_2–halloysite nanotubes and their visible light photocatalytic activity, J. Mater. Chem. A 1 (2013) 8045–8054.
[65] X. Liu, H. Cao, J. Yin, Generation and photocatalytic activities of Bi@Bi_2O_3 microspheres, Nano Res. 4 (2011) 470–482.
[66] J.N. Niu, A.C. Wu, D.X. Wang, L. Zhou, S.H. Zhang, Z.S. Li, P.Z. Peng, X.M. Ou, Y. H. Qiang, Coloading of TiO_2 and C_3N_4 on kaolinite nanotubes for obviously improved photocatalytic performance in degradation of methylene blue dye, Mater. Lett. 230 (2018) 32–35.
[67] J.C. Groen, L.A.A. Peffer, J. Perez-Ramirez, Pore size determination in modified micro- and mesoporous materials. Pitfalls and limitations in gas adsorption data analysis, Microporous Mesoporous Mater. 60 (2003) 1–17.
[68] A.N. Mansour, B.C. Beard, D.T. Cronce, R.P. Brown, Fluorescein by XPS, Surf. Sci. Spectra 1 (1992) 301–305.
[69] J. Moulder, W. Stickle, P. Sobol, Poly (ethyl methacrylate) by XPS, Surf. Sci. Spectra 1 (1992) 346–350.
[70] S. Akhter, X. Zhou, J. White, XPS study of polymer/organometallic interaction: trimethyl aluminum on polyvinyl alcohol polymer, Appl. Surf. Sci. 37 (1989) 201–216.
[71] D. Gonbeau, C. Guimon, G. Pfister-Guillouzo, A. Levasseur, G. Meunier, R. Dormoy, XPS study of thin films of titanium oxysulfides, Surf. Sci. 254 (1991) 81–89.
[72] B.V. Crist, Handbook of Monochromatic XPS Spectra: The Elements of Native Oxides, John Wiley & Sons, West Sussex, 2000.
[73] B. Afsin, M. Roberts, Formation of an oxy-chloride overlayer at a Bi (0001) surface, Spectrosc. Lett. 27 (1994) 139–146.
[74] W.E. Morgan, W.J. Stec, J.R. Van Wazer, Inner-orbital binding-energy shifts of antimony and bismuth compounds, Inorg. Chem. 12 (1973) 953–955.
[75] K. Burridge, J. Johnston, T. Borrmann, Silver nanoparticle–clay composites, J. Mater. Chem. 21 (2010) 734–742.
[76] S. Stepanov, V. Nikolaev, V. Bougrov, A. Romanov, Gallium OXIDE: properties and applica 498 a review, Rev. Adv. Mater. Sci. 44 (2016) 63–86.
[77] J. Nisar, C. Århammar, E. Jämstorp, R. Ahuja, Optical gap and native point defects in kaolinite studied by the GGA-PBE, HSE functional, and GW approaches, Phys. Rev. B 84 (2011), 075120.
[78] F. Zhang, K. Saito, T. Tanaka, M. Nishio, M. Arita, Q. Guo, Wide bandgap engineering of $(AlGa)_2O_3$ films, Appl. Phys. Lett. 105 (2014), 162107.
[79] X.L. Liang, Z.S. He, Y.H. Zhong, W. Tan, H.P. He, P. Yuan, J.X. Zhu, J. Zhang, The effect of transition metal substitution on the catalytic activity of magnetite in heterogeneous Fenton reaction: in interfacial view, Coll. Surf. A 435 (2013) 28–35.
[80] M.W. Laipan, R.L. Zhu, J.X. Zhu, H.P. He, Visible light assisted Fenton-like degradation of Orange II on Ni_3Fe/Fe_3O_4 magnetic catalyst prepared from spent FeNi layered double hydroxide, J. Mol. Catal a-Chem 415 (2016) 9–16.
[81] R. Beranek, (photo)electrochemical methods for the determination of the band edge positions of TiO_2-based nanomaterials, Adv. Phys. Chem. 2011 (2011), 786759.
[82] S. Gim, J. Bisquert, F. Principles, A. Devices, Photoelectrochemical solar fuel production, Photoelectrochem. Sol. Fuel Prod. (2016) 189–194.
[83] J.N. Niu, J. Albero, P. Atienzar, H. Garcia, Porous single-crystal-based inorganic semiconductor photocatalysts for energy production and environmental remediation: preparation, modification, and applications, Adv. Funct. Mater. 30 (2020) 1908984.
[84] D. Jiang, Z. Liu, L. Fu, H. Jing, H. Yang, Efficient nanoclay-based composite photocatalyst: the role of nanoclay in photogenerated charge separation, J. Phys. Chem. C 122 (2018) 25900–25908.